The RESEARCH LABORATORY

of

ELECTRONICS

at the

MASSACHUSETTS INSTITUTE OF TECHNOLOGY
CAMBRIDGE, MASSACHUSETTS 02139

A Circuit for Diffusive Breast Imaging and a Numerical Algorithm for its Inverse Problem

Julie L. Wonus and John L. Wyatt, Jr.

A Circuit for Diffusive Breast Imaging and a Numerical Algorithm for its Inverse Problem

Julie L. Wonus and John L. Wyatt, Jr.

RLE Technical Report No. 602

July 1996

The Research Laboratory of Electronics
MASSACHUSETTS INSTITUTE OF TECHNOLOGY
CAMBRIDGE, MASSACHUSETTS 02139-4307

A Circuit Model for Diffusive Breast Imaging and a Numerical

Algorithm for its Inverse Problem

Julie L. Wonus

John L. Wyatt

Abstract

This paper investigates the use of visible or near infrared light for breast cancer imaging. The use of light at this frequency avoids the potential danger of ionizing radiation from frequent mammographic screening. This method is inexpensive and harmless and is potentially attractive since it could be used more frequently than X-ray mammography, increasing the chances of early detection and successful treatment.

The hardware required consists of a movable light source, or multiple sources, and many detectors. The light is incident upon one side of the tissue and is measured at the opposite side. In addition, mathematical computations are required for the discrimination of cancerous tissue from normal tissue. Tumors are known to both scatter and absorb light *more* than average, and tissue immediately surrounding the tumor scatters and absorbs light slightly *less* than average, making the distinction possible [1,2].

Because tissue is dense with particles, photons which travel through it experience many collisions which scatter them [3, Chapter 7]. Although the material in a tumor is more highly scattering *and* absorbing than regular tissue, this research will focus on detection of changes in absorption *only*. In the circuit model, the absorption component is simpler to resolve than the scattering component, and when choosing a single parameter to begin reconstructing, its predictable increase is a simpler goal [14]. I may also be able to tag cancerous tissue with a highly absorbing material which would make the absorption extremely distinct in that area.

If there is a significant change in scattering or absorption, the measured light intensity is barely altered. This is the insensitive forward problem. Similarly, if the measurement of light intensity is slightly noisy and I attempt to solve for the unknown absorption or scattering, this computed perturbation may be mistakenly large, since there may have been no change at all.

Also, from a single source at the input and all the corresponding output measurements, we cannot assemble as many equations as there are unknowns. Even if the number of sources and resulting measurements is increased so that we have the same number of equations as unknowns, all of the equations will not be independent, and there is still not enough information to solve for all the unknowns. We therefore try to assemble many more equations than there are unknowns. This is done by increasing the number of unique input sources, each with their own set of output measurements, by as many as possible. The hope is that in making many measurements under different illuminations and accumulating more equations, some of the equations will be independent of the others that we already have, and it will help to resolve information about the problem out of noise.

Beginning with a nominal solution of uniform scattering and absorption, we can linearize the given, nonlinear, problem and iteratively update our guess at its solution. Since we assemble more equations than we have unknowns, we

search for the least squares solution to the nonlinear problem by iteratively solving a linearized perturbation equation.

This study will examine the underdetermined nature of the problem, and how that can be remedied. The result is that the accuracy of least squares solutions and performance of numerical algorithms are improved by adding regularization [8]. Other results include the success of the correspondence between the simulated circuit model and experimental data, and how much an increase in the number of illumination sites improves the resolution of the solution. The conclusion addresses what we can hope to resolve with this type of experimental system, and how much device noise can be tolerated in the apparatus.

Table of Contents

1. Light Transport Theory and Dense Media

The nature of light propagation is dependent upon the optical properties of the medium which it is traversing. When a medium has a refractive index of about one, particles are sparse within the medium and propagating photons follow an approximately straight line. In this case, light is usually not scattered or it experiences only one collision with a particle. If the medium has a slightly higher particle density, light is scattered just a few times and the multiple scattering can be approximated by a single scattering with an attenuation of both the incident wave and the scattered wave [3, Chapter 4].

Neither of these assumptions holds in the problem under study since it involves tissue. Because tissue is a dense medium, the majority of propagating photons will be scattered several times. We have a notion of the average distance light travels before colliding with another particle in the medium, and for dense media, there are many collisions between the incidence and exitance of photons [4]. We enter the world of multiple scattering events and blurry images.

The inadequacy of the two simpler models motivates a more rigorous investigation of photon propagation. The following paragraphs illustrate the fundamental concepts of light transport theory and its mathematical transition to the diffusion approximation, as presented by Ishimaru [3, Chapters 4, 7, and 9].

1.1 Diffusion Approximation

When a medium is appropriately dense, we can use the diffusion approximation and are exempted from solving the complete transfer equation of transport theory, Equation 1.2 below. In order to make this simplified approximation and have it produce accurate results, photon transport within the tissue must be dominated by scattering (a particle density issue), the medium must be several scattering lengths across in order to allow for multiple collisions,

the source must be at a distinct point in space and time, and the medium must be infinite[1]. This last constraint can be bypassed for our purposes by assuming that the source which is incident along the surface of a medium is actually a point source, and it originates at least one scattering length within the surface [10, 11].

Intensity refers to brightness or radiance of light. It may be measured radiating outward from a point or inward toward one. Two components of intensity are relevant here, and we begin with their definitions.

The *reduced incident intensity* is the component due to the original source of photons. It decreases exponentially due to the optical parameters known as scattering and absorption, and is governed by the following differential equation:

$$\frac{dI_{ri}(r,\hat{s})}{ds} = -\rho\sigma_t I_{ri}(r,\hat{s}), \qquad (1.1)$$

where r is the vector which defines the location of intensity and $\hat{s}$ is its direction of propagation. If we define the space constant to be the distance over which there is a decay in intensity by a factor of 1/e, where e is the exponential function, then we can further define the total cross section to be the inverse of the space constant in Equation 1.1, where the space constant is $1/\rho\sigma_t$. The total cross section, $\rho\sigma_t$, is the absorption coefficient per volume concentration plus the scattering coefficient per concentration: $\sigma_t = \sigma_a + \sigma_s$, multiplied by the volume density, ρ.

The *diffuse intensity* originates within the medium due to scattering. It is a sort of equivalent source. In the process of deriving the diffusion approximation, we will solve for the *average diffuse intensity*, from which we can substitute into a related equation to solve for the diffuse flux.

The *total intensity* within a random medium is equal to the sum of the reduced incident intensity (I_{ri}) plus the diffuse intensity (I_d). The total intensity satisfies the following well-known transfer equation:

---

[1] Scattering length will be defined in Section 1.2.

$$\frac{dI(r,\hat{s})}{ds} = -\rho\sigma_t I(r,\hat{s}) + \frac{\rho\sigma_t}{4\pi}\int_{4\pi} p(\hat{s},\hat{s}')I(r,\hat{s}')d\omega' + \varepsilon(r,\hat{s}). \qquad (1.2)$$

Since we define total intensity as the sum of reduced incident intensity plus diffuse intensity, we can substitute this sum into Equation 1.2 to get the following differential transfer equation of *diffuse* transfer:

$$\frac{dI_d(r,\hat{s})}{ds} = -\rho\sigma_t I_d(r,\hat{s}) + \frac{\rho\sigma_t}{4\pi}\int_{4\pi} p(\hat{s},\hat{s}')I_d(r,\hat{s}')d\omega' + \varepsilon_{ri}(r,\hat{s}) + \varepsilon(r,\hat{s}), \qquad (1.3)$$

where:

$$\varepsilon_{ri}(r,\hat{s}) = \frac{\rho\sigma_t}{4\pi}\int_{4\pi} p(\hat{s},\hat{s}')I_{ri}(r,\hat{s}')d\omega' \qquad (1.4)$$

is referred to as the equivalent source function due to the reduced incident intensity, $\varepsilon(r,\hat{s})$ is the original source function [3, Chapter 7], and we eliminate equivalent components of reduced incident intensity according to Equation 1.1. There is also a related boundary condition since diffuse intensity is generated only within the medium: along a surface of solid angle, no diffuse intensity enters the medium; for $\hat{s}$ pointing inward through the surface,

$$I_d(r,\hat{s}) = 0. \qquad (1.5)$$

We assume that the diffuse intensity is approximately equal to a sum of the average diffuse intensity, which is radially symmetric, plus a fraction of the diffuse power flux. This bias toward the diffuse power flux allows for net power propagation in the forward direction; there would be no net propagation if the diffuse intensity were constant over all directions.[2] The following calculation uses established relations to solve for the constant c, the approximate bias of diffuse intensity in the direction of diffuse power flux.

The diffuse flux is the vector of net power flux in the direction $\hat{s}_f$:

---

[2] Later we will introduce a separate constant which deals with the anisotropy of the scattering events.

$$\mathbf{F}_d(\mathbf{r}) = F_d(\mathbf{r})\hat{\mathbf{s}}_f = \int_{4\pi} I_d(\mathbf{r},\hat{\mathbf{s}})\hat{\mathbf{s}}d\omega \ . \qquad (1.6)$$

The average diffuse intensity over the entire solid angle is defined as:

$$U_d(\mathbf{r}) = \frac{1}{4\pi}\int_{4\pi} I_d(\mathbf{r},\hat{\mathbf{s}})d\omega . \qquad (1.7)$$

As suggested, we assume that the diffuse intensity is a sum of the average diffuse intensity, $U_d(\mathbf{r})$, plus a fraction of the diffuse flux vector, $\mathbf{F}_d(\mathbf{r})$, giving the diffuse intensity a bias along $\hat{\mathbf{s}}_f$ which is felt in its dot product with the direction of intensity propagation, $\hat{\mathbf{s}}$, as we take its projection in that direction:

$$I_d(\mathbf{r},\hat{\mathbf{s}}) \approx U_d(\mathbf{r}) + c\mathbf{F}_d(\mathbf{r})\cdot\hat{\mathbf{s}}. \qquad (1.8)$$

We will express this equation in terms of the diffuse flux only, and thereby solve for c. This is done by substituting the right hand side of Equation 1.8 into Equation 1.6 to get:

$$\mathbf{F}_d(\mathbf{r}) = \int_{4\pi} U_d(\mathbf{r})\hat{\mathbf{s}}d\omega + c\int_{4\pi}(\mathbf{F}_d(\mathbf{r})\cdot\hat{\mathbf{s}})\hat{\mathbf{s}}d\omega. \qquad (1.9)$$

We then use the following integral relation: for any vector **A**,

$$\int_{4\pi} \hat{\mathbf{s}}(\hat{\mathbf{s}}\cdot\mathbf{A})d\omega = \frac{4\pi\mathbf{A}}{3}. \qquad (1.10)$$

This relation helps us to integrate the second term on the right hand side of Equation 1.9. The first term on the right hand side goes to zero since it is a constant multiplied by $\sin(\varphi)$: φ is the angle between the direction of intensity, $\hat{\mathbf{s}}$, and each point of integration on the sphere; and over all φ the integral of a constant times sine is zero. This gives:

$$\mathbf{F}_d(\mathbf{r}) = c\frac{4\pi\mathbf{F}_d(\mathbf{r})}{3}.$$

The result is that $c = 3/4\pi$, and the diffuse intensity is approximated as:

$$I_d(\mathbf{r},\hat{\mathbf{s}}) \approx U_d(\mathbf{r}) + \frac{3}{4\pi}\mathbf{F}_d(\mathbf{r})\cdot\hat{\mathbf{s}}. \qquad (1.11)$$

We will assume equality in this approximation for the rest of the derivation. It will be used in an approximation to the diffuse transfer equation.

The diffuse transfer equation is next integrated over 4π, the entire solid angle. This is a logical step considering Equation 1.7 and our motivation to express the transfer equation solely in terms of the average diffuse intensity. To do this we first take the gradient relation for $I_d(\mathbf{r},\hat{\mathbf{s}})$:

$$\frac{dI_d(\mathbf{r},\hat{\mathbf{s}})}{ds} = \hat{\mathbf{s}}\cdot\text{grad}I_d(\mathbf{r},\hat{\mathbf{s}}) = \text{div}[I_d(\mathbf{r},\hat{\mathbf{s}})\hat{\mathbf{s}}], \qquad (1.12)$$

and integrate the first and last terms above to get the first two terms of the next line:

$$\int_{4\pi}\frac{dI_d(\mathbf{r},\hat{\mathbf{s}})}{ds}d\omega = \text{div}[\int_{4\pi}I_d(\mathbf{r},\hat{\mathbf{s}})\hat{\mathbf{s}}d\omega] = \text{div}\mathbf{F}_d(\mathbf{r}). \qquad (1.13)$$

The last term above is due to Equation 1.6 and it becomes the left hand side of the integrated diffuse transfer equation, Equation 1.3. The right hand side is assembled in the next few steps.

Using Equation 1.7, the first term is $-4\pi\rho\sigma_t U_d$. For the next term we use the relation:

$$\frac{\sigma_s}{\sigma_t} = \frac{1}{4\pi}\int_{4\pi}p(\hat{\mathbf{s}},\hat{\mathbf{s}}')d\omega \qquad (1.14)$$

with Equation 1.7 to get $4\pi\rho\sigma_s U_d$. The third term on the right is $4\pi\rho\sigma_s U_{ri}$, due to Equations 1.4, 1.7, and 1.14 (but 1.7 for reduced incident intensity instead of diffuse intensity). The last term is the power generated per unit volume per unit frequency interval:

$$E(\mathbf{r}) = \int_{4\pi}\varepsilon(\mathbf{r},\hat{\mathbf{s}})d\omega. \qquad (1.15)$$

Summing the terms which belong to the right hand side, the first two become one term and the integrated diffuse transfer equation is:

$$\text{div}\mathbf{F}_d(\mathbf{r}) = -4\pi\rho\sigma_a U_d(\mathbf{r}) + 4\pi\rho\sigma_s U_{ri} + E(\mathbf{r}). \qquad (1.16)$$

We can substitute the approximate diffuse intensity given in Equation 1.11 into the differential diffuse transfer equation, Equation 1.3. Instead of the derivative on the left hand side of Equation 1.3, we use the gradient term, the second term in Equation 1.12, along with Equation 1.14 and Equation 1.18, below, to get:

$$\hat{s}\cdot\text{grad}\,U_d + \frac{3}{4\pi}\hat{s}\cdot\text{grad}(F_d\cdot\hat{s}) = -\rho\sigma_t U_d - \frac{3}{4\pi}\rho\sigma_t F_d\cdot\hat{s} + \rho\sigma_s U_d + \frac{3}{4\pi}\rho\sigma_t p_1 F_d\cdot\hat{s} + \varepsilon_{ri} + \varepsilon\cdot \tag{1.17}$$

The integral of the phase function, $p(\hat{s},\hat{s}')$, is the amount of net forward scattering (the scattering can have a forward bias, just as the power flux did):

$$p_1 = \frac{1}{4\pi}\int_{4\pi}p(\hat{s},\hat{s}')\hat{s}\cdot\hat{s}'d\omega' \ . \tag{1.18}$$

Now we multiply Equation 1.17 by $\hat{s}$ and integrate over the solid angle $d\omega$. The first and third terms on the right hand side go to zero because of the multiplication by $\sin(\varphi)$, as before. The second and fourth terms on the right hand side combine into one. Use the following relation to get rid of the second term on the left hand side: for any vector A,

$$\int_{4\pi}\hat{s}(\hat{s}\cdot\text{grad}(\mathbf{A}\cdot\hat{s}))d\omega = 0\ . \tag{1.19}$$

Use Equation 1.10 to integrate the rest of the equation. The result is:

$$\frac{4\pi}{3}\text{grad}\,U_d = -\rho\sigma_t(1-p_1)F_d + \int\varepsilon_{ri}(\mathbf{r},\hat{s})\hat{s}\,d\omega + \int\varepsilon(\mathbf{r},\hat{s})\hat{s}\,d\omega\ . \tag{1.20}$$

Eliminate $F_d(\mathbf{r})$ from Equation 1.20 by taking the divergence of the rest of Equation 1.20, dividing through by the coefficient of $F_d(\mathbf{r})$, and setting the resultant expression for $\text{div}(F_d(\mathbf{r}))$ equal to the right hand side of Equation 1.16. We also use a few other substitutions. The transport cross section is the *scaled* total cross section:

$$\sigma_{tr} = \sigma_t(1-p_1) = \sigma_s(1-\bar{\mu}) + \sigma_a\,, \tag{1.21}$$

and $\bar{\mu} = \hat{s}\cdot\hat{s}'$ is the anisotropy factor, the mean cosine of the scattering angle. Biological tissue is highly forward scattering and $\bar{\mu}$ is typically between 0.945

10

and 0.985 for breast tissue [45, p. 1328]. If we use the transport cross section in lieu of the total cross section, we can assume that the medium is isotropic in scattering since this term compensates for the anisotropy. Another helpful constant is:

$$\kappa_d^2 = 3\rho^2 \sigma_a \sigma_{tr}. \qquad (1.22)$$

The resultant equation is:

$$\nabla^2 U_d(\mathbf{r}) - \kappa_d^2 U_d(\mathbf{r}) = -3\rho^2 \sigma_s \sigma_{tr} U_{ri}(\mathbf{r}) - \frac{3}{4\pi}\rho\sigma_{tr}E(\mathbf{r}) + \frac{3}{4\pi}\nabla \cdot \int_{4\pi} \varepsilon_{ri}(\mathbf{r},\hat{\mathbf{s}})\hat{\mathbf{s}}d\omega + \frac{3}{4\pi}\nabla \cdot \int_{4\pi} \varepsilon(\mathbf{r},\hat{\mathbf{s}})\hat{\mathbf{s}}d\omega \qquad (1.23)$$

The simplification of this equation which is relevant to our research problem involves the assumption of a point source incident upon a slab of particles. In this case the actual input source, $\dot{\varepsilon}(\mathbf{r},\hat{\mathbf{s}})$, is the original source reduced over one scattering length and incident at one scattering length within the boundary. We neglect the reduced incident intensity terms. The diffuse transfer equation is then:

$$\nabla^2 U_d(\mathbf{r}) - \kappa_d^2 U_d(\mathbf{r}) = -3\rho\sigma_{tr}\varepsilon(\mathbf{r},\hat{\mathbf{s}}). \qquad (1.24)$$

Equation 1.24 is the time-independent diffusion approximation in its most familiar form. It is easily converted to a discrete matrix relation by using an approximation to the discrete second spatial derivative. It also is translated to a time-dependent diffusion equation by subtracting a time derivative of $U_d(\mathbf{r})$ from the term which is linear in $U_d(\mathbf{r})$, on the left hand side of Equation 1.24 [25]. A higher-order approximation, the diffusive wave approximation, can be investigated elsewhere [12], but the validity of the diffusion approximation in the range of coefficients which are characteristic of biological media has been established using Monte Carlo methods [11].

1.2 Scattering Length

11

A prominent measure in this study is the scattering length, the space constant for the problem when we assume it is isotropic, and the inverse of the transport cross section. This parameter is composed of the scattering and absorption coefficients, and the average scattering angle. In tissue, the coefficient of absorption is typically much less than the coefficient of scattering for frequencies of light in the near infrared range [10].

Just as the heat flux in heat flow problems, in order for diffusion to occur, *particles* (photons in our case) must travel beyond the distance in which collisions, solely, dominate their motion. That assumes migration across a distance of many scattering lengths. This photon behavior is governed by nearly the same equation that is used for the kinetic theory of gases, Boltzmann's equation or the Maxwell-Boltzmann collision equation. There is an added loss term which may account for photons which fall out of the problem for our purposes.

We can physically relate this problem to one based on the second-order equations for heat flow if the absorbers within the tissue are seen as cold plates inserted within the field of thermodynamic heat flow [14]. This is an analog of the diffusion approximation since it relies on transport theory for its particle relationships and since the diffusion approximation resembles the second-order time-dependent differential equation of heat transfer:

$$\nabla \cdot K_o \nabla u - c\rho \frac{\delta u}{\delta t} = -Q.$$

With the loss term we have the time-dependent diffusion approximation [15]. The form of the equation above is therefore analogous to the *lossless* diffusion equation, whereas we are concerned with the *lossy* diffusion equation [32].

1.3 Measurement models

Different measurement methods are being researched for this application of optical tomography. We address the continuous wave model, in which the

input signal is of constant intensity and the output is measured in terms of steady state photon flux. In time-resolved measurements, the input is a short pulse which simulates a delta function and the measured output is a time-dependent photon flux. In a third type of measurement model, the photon fluxes are time-gated at the output in order to count only the earliest arriving photons. A fourth measurement model requires a periodic source function whose measured output varies from the input wave in phase and amplitude, depending on the internal structure of the medium. This last measurement model is related to the time-dependent results by a Fourier transform.

The continuous-wave data is easy to simulate, but studies show that it may be easier to resolve images at greater depth with higher-order data [25, Section 9]. The idea of time-gated data suggests a more coherent passage from source to detector, which might offer a clearer reconstruction of the model's interior parameters. But these more coherent photons are difficult to measure since they have the fastest arrival times at the output and require the use of superfast imaging processes such as streak cameras. Also note that because of their early arrival times and probable short propagation paths, these photons have not traveled far enough through the medium to be considered in the diffusion approximation.

2. Two-Dimensional Circuit Models for Diffusive Light Transfer

This chapter translates the light intensity input from Chapter 1 to a current injection. The intensity measured at the output is now a voltage potential. The medium between them is modeled as a resistive sheet. Although it is not intuitive to model photons, which propagate in waves, as electrons within circuitry, their diffuse behavior allows us to make the conceptual step to the elliptic partial differential equation. This differential equation, derived in Chapter 1, is approximated well by the resistive sheet.

Our simplest model of the problem is this two-dimensional, rectangular cross section of tissue. The discretized version of the resistive sheet models the rectangular cross section and is shown in Figure 3.1. Throughout this research, the edges of the grid are open-circuited; wrapping the 'top' edge around to the 'bottom' edge introduces additional, unwanted, symmetry into the problem. There is a line of input current along one edge of the rectangle. Voltage decays spatially across the sheet and a line of output potentials forms the opposite edge of the rectangle.

2.1 Continuous Model

We begin to define the continuous version of the resistive circuit model by describing its properties over one dimension, and then progressing to two dimensions later in this section. Both treatments originate in the text by Mead [17]. In the first treatment, We isolate a one-dimensional line of the two-dimensional sheet, from one input node to one output node. The second treatment takes the resistive line to the two-dimensional resistive sheet.

Consider the case when a potential V_o is applied at the left side of the sheet, where $x = 0$. The resistance along a line approaching $x = \infty$ is equal to R Ohms per unit length. The conductance to ground is G mho per unit length [17].

The current at location x+dx is directed to the right; it is multiplied by the resistance seen between x and x+dx (which is R times the length dx) and a negative sign to specify that charge is traveling away from x to x+dx. The result is the potential difference between x and x+dx:

$$-I(x+dx)Rdx = V(x+dx) - V(x).$$

Dividing both sides by dx gives:

$$\frac{V(x+dx) - V(x)}{dx} = -\frac{I(x+dx)Rdx}{dx}.$$

V attains a differential relationship as dx approaches 0, and we get:

$$\frac{dV}{dx} = -IR. \qquad (2.1)$$

Differentiating Equation 2.1 once more with respect to x gives:

$$\frac{d^2v}{dx^2} = -\frac{dI}{dx}R,$$

and after rearranging terms this becomes:

$$\frac{dI}{dx} = -\frac{1}{R}\frac{d^2V}{dx^2} \qquad (2.2).$$

Similarly, the current to the right at location x+dx is equal to the current at location x minus the loss of current to ground over dx, which is V(x)Gdx:

$$I(x+dx) = I(x) - V(x)Gdx.$$

As dx approaches zero and:

$$\frac{I(x+dx) - I(x)}{dx} = -\frac{V(x)Gdx}{dx}, \qquad (2.3)$$

we have that:

$$\frac{dI}{dx} = -VG \qquad (2.4)$$

Setting Equations 2.2 and 2.4 equal gives:

$$\frac{d^2V}{dx^2} = RGV.$$

The known solution to this second order differential equation is:

$$V = V_0 e^{-\alpha x} \, ,$$

where $1/\alpha$ is the resistive space constant and

$$\alpha = \sqrt{RG} \, ,$$

the inverse of the resistive scattering length [17]. There would be an *increasing* exponential term as well, but we know that the potential must converge toward a nonnegative value with increasing distance along the resistive line, so we include only the *decreasing* exponential term.

When we progress to two dimensions, the differential equation governing the potential along the sheet is:

$$\frac{d^2V}{dr^2} + \frac{1}{r}\frac{dV}{dr} - \alpha^2 V = 0 \, ,$$

where once again α, the inverse of the space constant, is $\pm\sqrt{RG}$ [17]. The radial (θ) dependency is neglected because we assume uniform optical parameters for this two-dimensional continuous sheet of tissue material, so that the propagation is radially symmetric. Now, R is the sheet resistance in Ohms per square and G is the conductance to ground in mho per unit area [17].

The well-known modified Bessel function solution to this differential equation on an infinite sheet of material is:

$$V = V_0 K_0(\alpha r) \, .$$

The modified Bessel function can be approximated as:

$$K_0(\alpha r) \approx -\ln(\alpha r), \quad \alpha r \ll 1 \qquad (2.5)$$

$$K_0(\alpha r) \approx \sqrt{\frac{\pi}{2\alpha r}} e^{-\alpha r}, \quad \alpha r \gg 1 \qquad (2.6)$$

on a ring of radius r. If we assume that our resistive sheet is infinite, which is approximately true if we are a few scattering lengths inside the surface, an elegant formulation for the attenuation of potential can be derived, as shown below. This attenuation result is a key conceptual ingredient in this research, and we will be referring back to it as it becomes needed.

Assume we are in the region where the distance r between the node and

16

a source or detector is much greater than a space constant, $1/\alpha$. Identify three points on the resistive sheet, $r_0, r_1,$ and r_2 , where each r represents a different set of coordinates (x,y). These are shown in Figure 2.1 below. Let r_0 be a point
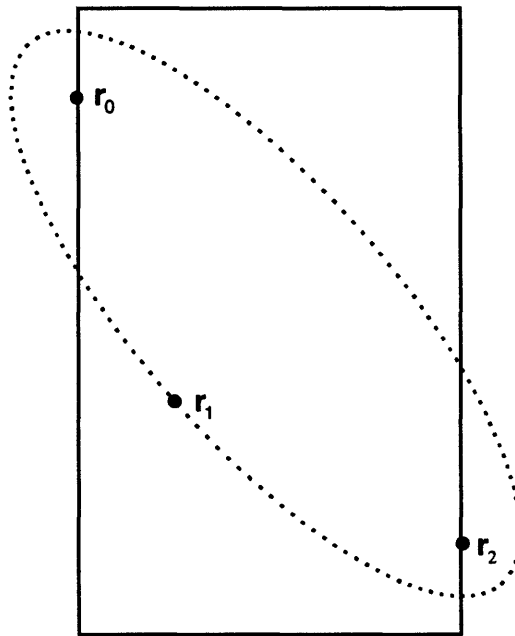
Figure 2.1: An Ellipse of Constant Influence

at which we inject a current source onto the resistive sheet. The point r_2 is a location at which we are interested in measuring the change in potential due to an increase in the conductance to ground at the point r_1 . Using the fact that:

$$\frac{\delta V}{\delta r} = -I\frac{R}{2\pi r}, \qquad (2.7)$$

along with the assumption that, when r is very small, we can differentiate Equation 2.5 to get that the change in potential which we inject is:

17

$$\frac{\delta V}{\delta r} = -\frac{V_o}{r}, \qquad (2.8)$$

Substituting Equation 2.7 into Equation 2.8 and solving for I, the I_o which will induce the source term V_o, gives:

$$V_o = \frac{I_o \rho}{2\pi}.$$

Driving with a current equal to I_o at the source location r_0 results in a potential value at r_1 which is approximately equal to the modified Bessel function evaluated at $\alpha r = \alpha \| r_1 - r_0 \|$ times the input potential V_o which is: $V_o K(\alpha \| r_1 - r_0 \|)$.

The final output potential measured at r_2 can also be approximated by the modified Bessel function. We assume that a 'source' $V_o K(\alpha \| r_1 - r_0 \|)$ is incident at r_1 and decays to a potential which we measure at r_2. We can thus represent the current output at r_2 by a two-dimensional convolution [14, 20]:

$$I(r_2) = \iint \delta G(r_1) K_o(\alpha \| r_2 - r_1 \|) V_o K_o(\alpha \| r_1 - r_0 \|) dr. \qquad (2.9)$$

Using the approximation to the modified Bessel function in Equation 2.6, the equation above can be rewritten as:

$$I(r_2) \approx \iint \delta G(r_1) \sqrt{\frac{\pi}{2\alpha \| r_2 - r_1 \|}} \exp(-\alpha \| r_2 - r_1 \|) V_o \sqrt{\frac{\pi}{2\alpha \| r_1 - r_0 \|}} \exp(-\alpha \| r_1 - r_0 \|) dr,$$

assuming that we are far inside any boundaries, so that the assumption of an infinite medium still holds, and $\alpha r \gg 1$. If the relative contributions of the terms proportional to $\sqrt{\frac{1}{r}}$ are assumed to be approximately the same for different sets of r's, then we can isolate the dependence of the output current on the exponential terms:

$$I(r_2) \approx \iint \delta G(r_1) \exp(-\alpha \| r_2 - r_1 \|) V_o \exp(-\alpha \| r_1 - r_0 \|) dr,$$

18

which means that the potential will be proportional to the sum of the distances $\|r_1 - r_0\|$ and $\|r_2 - r_1\|$:

$$V(r_2) \propto \iint \delta G(r_1) V_o \exp[-\alpha(\|r_1 - r_0\| + \|r_2 - r_1\|)] dr. \qquad (2.10)$$

At each point, r_1, within the medium which we are isolating to analyze the extent to which the measured potential at r_2 depends on $\delta G(r_1)$, there are ellipses along a collection of r_1's which produce a sum, $\|r_1 - r_0\| + \|r_2 - r_1\|$, which is equal everywhere along the ellipse, as in Figure 2.1 [14, 20, 48]. According to Equation 2.10, those r_1's have a constant influence on $V(r_2)$. We'll refer back to the integral product in Equation 2.10 later in the text as the source of a Jacobian of the output potentials with respect to the change in vertical conductances at every node along the grid, and as a rationalization for near-zero changes in the output potential due to perturbations along these ellipses of constant influence.

2.2 Discrete Model

The discrete model consists of a grid of node voltages which are connected by resistors between each node and its four nearest neighbors, and by resistors from each node to ground. The discretization is necessary in order to make computer modeling possible, and coarser discretizations are more computationally optimal since they facilitate a more efficient usage of memory and leave us with less unknown parameters for which to solve.[3]

The resistor values depend on the area of the grid belonging to each node, and on the mean scattering angle and the absorption and scattering coefficients. The spacing between nodes is the same in both directions, in order to preserve isotropic behavior in the model. If we compare the electric potential

---

[3] This is, of course, assuming that the discretization is fine enough to provide an adequate quantity and localization of information.

at a discrete node, $u_{i,j}$, with the average diffuse intensity, $U_d(r)$, at the corresponding value of r, then the homogeneous part of the time-independent diffusion approximation is:

$$\nabla^2 u_{i,j} - \kappa_d^2 u_{i,j} = 0. \qquad (2.11)$$

Discretizing the Laplacian operator in Equation 2.11 and using the definition of κ_d^2 from Chapter 1 along with the generalized definition: $\mu_x \equiv \sigma_x \rho$, Equation 2.11 has the finite difference formulation:

$$\frac{(4u_{i,j} - u_{i,j-1} - u_{i,j+1} - u_{i-1,j} - u_{i+1,j})}{d^2} - 3\mu_a \rho \sigma_{tr} u_{i,j} = 0. \qquad (2.12)$$

Expanding Equation 2.12 according to the definition of $\rho \sigma_{tr}$, it becomes:

$$\frac{(4u_{i,j} - u_{i,j-1} - u_{i,j+1} - u_{i-1,j} - u_{i+1,j})}{d^2} - 3\mu_a \left[(1-\bar{\mu})\mu_s + \mu_a\right] u_{i,j} = 0. \qquad (2.13)$$

Now, if we assume that $\bar{\mu} \approx 0.95$, the second term in Equation 2.13 becomes:

$$-3\mu_a \left[.05 * \mu_s + \mu_a\right] u_{i,j}. \qquad (2.14)$$

If we move the expression in brackets in Equation 2.13 into the denominator of the first term of that equation, then the second term depends only on absorption and not on scattering. We would like to model this 'loss term' of the diffusion approximation with resistors to ground, since in both cases particles (photons or electrons) are absorbed and lost from the model. The first term of Equation 2.13 then looks a lot like a circuit's node equation, we would like to attribute it solely to scattering. This first term, however, depends on both scattering and absorption, due to the expression within brackets in Equation 2.14.

We can also move one of the d's from the denominator of the first term in Equation 2.13 to the numerator of the second term, so that both terms have a dependence upon the node spacing, d. We then have:

$$\frac{(4u_{i,j} - u_{i,j-1} - u_{i,j+1} - u_{i-1,j} - u_{i+1,j})}{d(.05 * \mu_s + \mu_a)} - 3\mu_a d u_{i,j} = 0. \qquad (2.15)$$

20

This operation is fairly arbitrary, but it leaves the coefficients of the u's dimensionless. The resultant form can be compared with Kirchoff's current law for the discrete resistive grid:

$$G_h(4u_{i,j} - u_{i,j-1} - u_{i,j+1} - u_{i-1,j} - u_{i+1,j}) + G_v u_{i,j} = i_{i,j} \ . \qquad (2.16)$$

The current, i, is zero at all grid nodes which are not along the input. The conductance G_h at a particular node is that due to resistors located 'horizontally' (in the plane of the node and its neighbors) adjacent to node [i,j] (the 'scattering' resistors), and G_v is the conductance due to resistors between each node and ground (the 'absorption' resistors), which take on a 'vertical' spatial relationship orthogonal to the plane of the node and its neighbors. As addressed in the preceding paragraph, these correspondences (of scattering to G_h and absorption to G_v) are not preserved when we solve for the G_h and G_v which make the coefficients in Equation 2.15 agree with those in Equation 2.16.

2.3 Validity of the Model

Simulations which are described in this section compare the experimental results of an undergraduate researcher, Jooyoun Park, with the results of our simulated model of the problem, based on the relationship between optical parameters and resistor values which is described above [7]. Jooyoun's experiments use a tank which is filled with 3-4% Intralipid-10%™ solution. The approximate scattering and absorption coefficients have been found experimentally for a 0.1% concentration of Intralipid-10%™ solution at a wavelength of 633 nm [43]. We used a linear interpolation to project the scattering and absorption coefficients from what they would be at the lower concentration to their values at the concentration she used in her experiments, since the literature indicates that the coefficients scale linearly with concentration [43].

We assume that there is a 3.5% concentration of Intralipid-10%™ solution (which means that the values for the 0.1% concentration will have to be scaled by a factor of thirty-five), and that the coefficients based on this wavelength will resemble Jooyoun's DC experiments. The parameters for both concentrations are given in Table 2.1, below. Values with a '≈' symbol next to them are ones which we calculated.

Concentration of Intralipid-10%™	Scattering Coefficient(mm^{-1})	Absorption Coefficient(mm^{-1})	Transport Cross Section(mm^{-1})	Anisotropy Constant
0.1%	$38.6\pm4 \times 10^{-3}$	$5.7\pm1.5 \times 10^{-5}$	$\approx.011251$	0.71 ± 0.03
3.5%	≈1.351	$\approx2.0 \times 10^{-3}$	≈0.392	0.71 ± 0.03

Table 2.1: Optical Parameters for two concentrations of Intralipid-10%™

To model the absorbers, Jooyoun uses glass rods which are 4mm in exterior diameter and 2mm in interior diameter. The rods are filled with methyl green dye. My simulations model the glass part of the rod with the same optical parameters as for the Intralipid-10%™. This is an approximation, but modeling the entire rod as an absorber would truly simulate an absorber of four times the actual area of absorbing material [49].

The absorption of the dye is unknown, but an estimate of 1000 mm^{-1} gives results which are fairly consistent with the experimental results. Increasing the absorption coefficient from this value has a negligible effect on the measured output potential: the corresponding conductance is so high that it is nearly a perfect short to ground. This figure is much higher than we would expect of cancerous tissue, but we also expect to be able to use biologically safe markers which attach themselves to cancerous tissue and have a highly absorbing effect.

The scattering coefficient of the green dye is assumed to be the same as that of the Intralipid-10%™ solution, and the detected output potential is only altered by a negligible amount when this scattering coefficient is further increased in the computer simulation. We did not experiment with decreasing it. The physical details of the experiments are described in the next few

paragraphs. We compare a slice of Jooyun's three-dimensional solutions with our two-dimensional resistive grid. A more precise description of the computer model is found in Chapter 3.

The experiments described below are all performed within a Plexiglas tank which is either one or two inches deep, twelve inches wide, and three inches high, and is filled with the Intralipid-10%™ solution. Each experiment addresses different configurations of two 'absorbers' which are also in the tank, and which distinguish themselves from experiment to experiment by being separated by different distances or by varying in their distance from the detector. Their separation is always symmetric about the center of the tank, and the two absorbers are always at equal distances from the detector. A two-dimensional picture, as if taken from above the tank, of a generic configuration is shown in Figure 2.2.

Figure 2.2: Arial view of a Plexiglas tank filled with Intralipid-10%™ solution and two glass rods filled with absorbing green dye.

Rods filled with absorbing green dye are inserted in four distinct experimental configurations in Jooyoun's study, and are illuminated with a .5 mW He laser light source along the edge in Figure 2.2 which is marked 'Input edge'. The output potential is measured with a photodiode amplifier along the 'Detector edge'.

Measurement noise should be due mostly to quantization, and our simulation therefore includes 8-bit quantization noise, to correspond to the equipment which was used in these experiments, assuming that the gain was set to optimally detect over the varying dynamic ranges at the output [35]. This can be done with knowledge of the expected nominal output potential – the measured output potential without any added absorption.

The first two experiments are performed on a tank which is one inch thick and filled with Intralipid-10%™ solution. Figure 2.3 shows the result of a simulation of two absorbers separated by 2 cm, and which are 1.2 cm from the detector edge. The experimental result, indicated by plusses, consisted of two dips in percent change in magnitude which were approximately 2 cm apart and at fifty-six and fifty-eight percent difference.[4] The relative peak between the dips was at thirty-eight percent difference in magnitude. The experimental results are closely approximated by the computer simulation, which is shown by the solid line.

Figure 2.4 is the experimental result of two absorbers which are 3 cm apart and 2 cm from the detector edge. Experiments produced two dips which are approximately 3 cm apart. The absorbers create dips in percent differences at sixty-eight and sixty-five percent, with a relative peak between them at about zero percent difference. Again, with the same symbolic plotting conventions, the computer simulation result is very similar.

The next two experiments are performed on a slab which is two inches deep. Figure 2.5 is a measurement taken from two absorbers which are 2 cm apart and 1.5 cm from the detector edge. Experiments produced one wide dip at fifty-eight percent difference in magnitude. The simulation even duplicates this *single dip*! Figure 2.6 is an output measurement resulting from two absorbers which are 3 cm apart and 1.5 cm from the detector side. Experiments produced two dips at a distance of 3 cm apart, with dips in percent differences at forty-

---

[4] The experimental results were described as having dips which had the same separation as the absorber locations, so we assume that they coincide with the actual absorber locations, and only plot one marker representing experimental results.
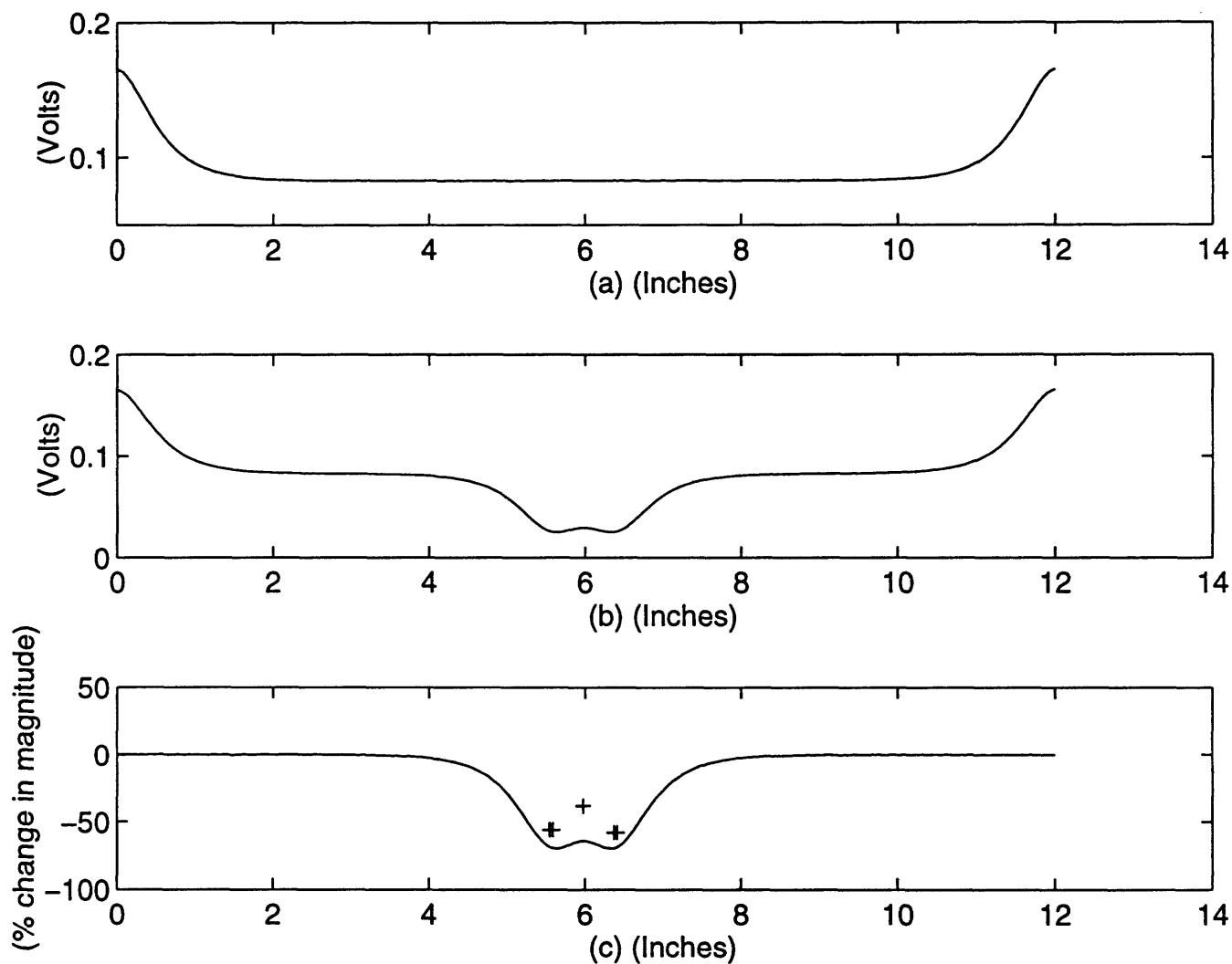
Figure 2.3: Two absorbers placed 2 cm apart and 1.2 cm away from the detector edge: computer simulation result (_) and experimental peak and dip locations (+); output potential due to nominal absorption (a), output potential with perturbation in absorption (b), and percent change in magnitude from the nominal to the perturbed case (c).
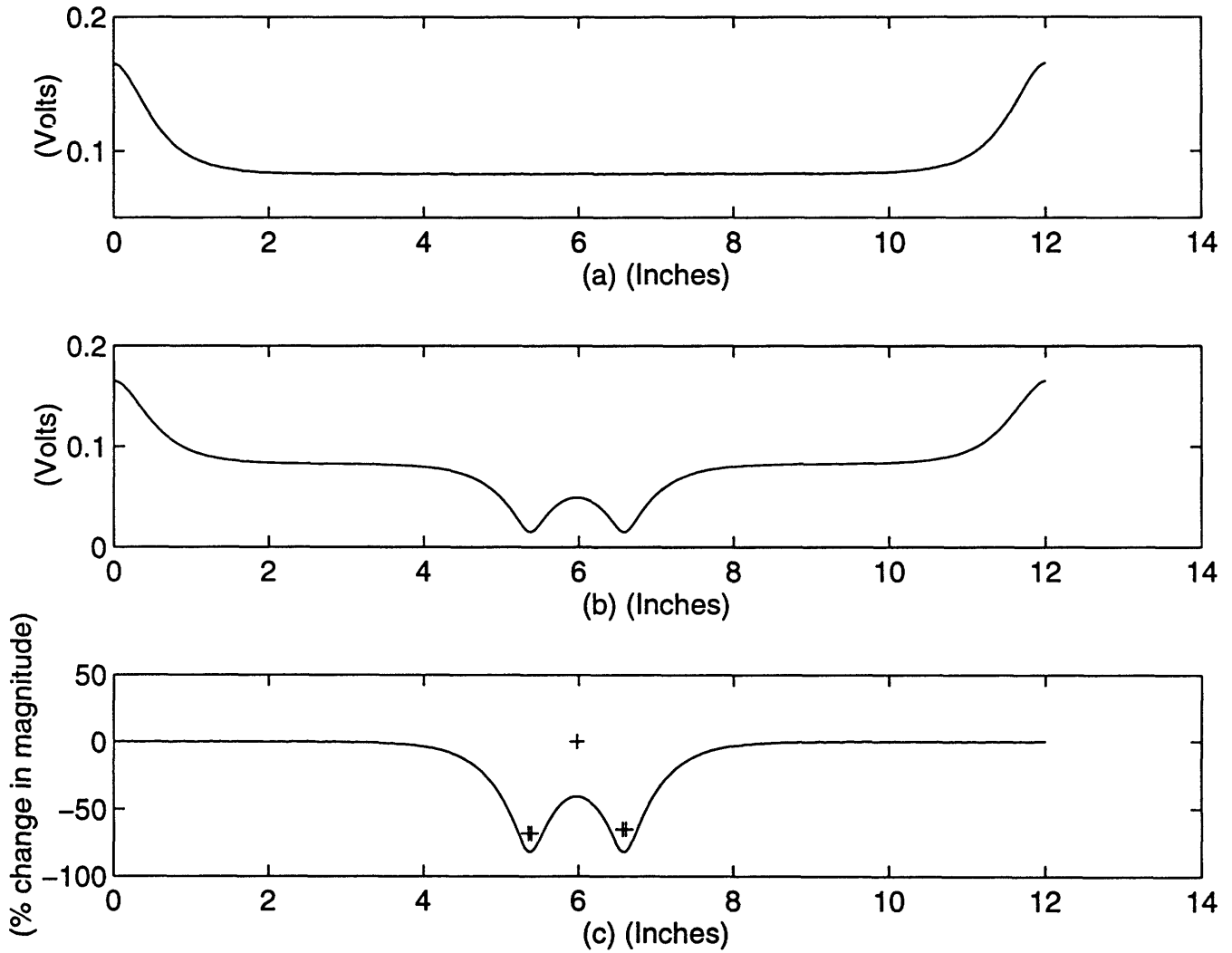
Figure 2.4: Two absorbers placed 3 cm apart and 2.0 cm away from the detector edge: computer simulation result (_) and experimental peak and dip locations (+); output potential due to nominal absorption (a), output potential with perturbation in absorption (b), and percent change in magnitude from the nominal to the perturbed case (c).
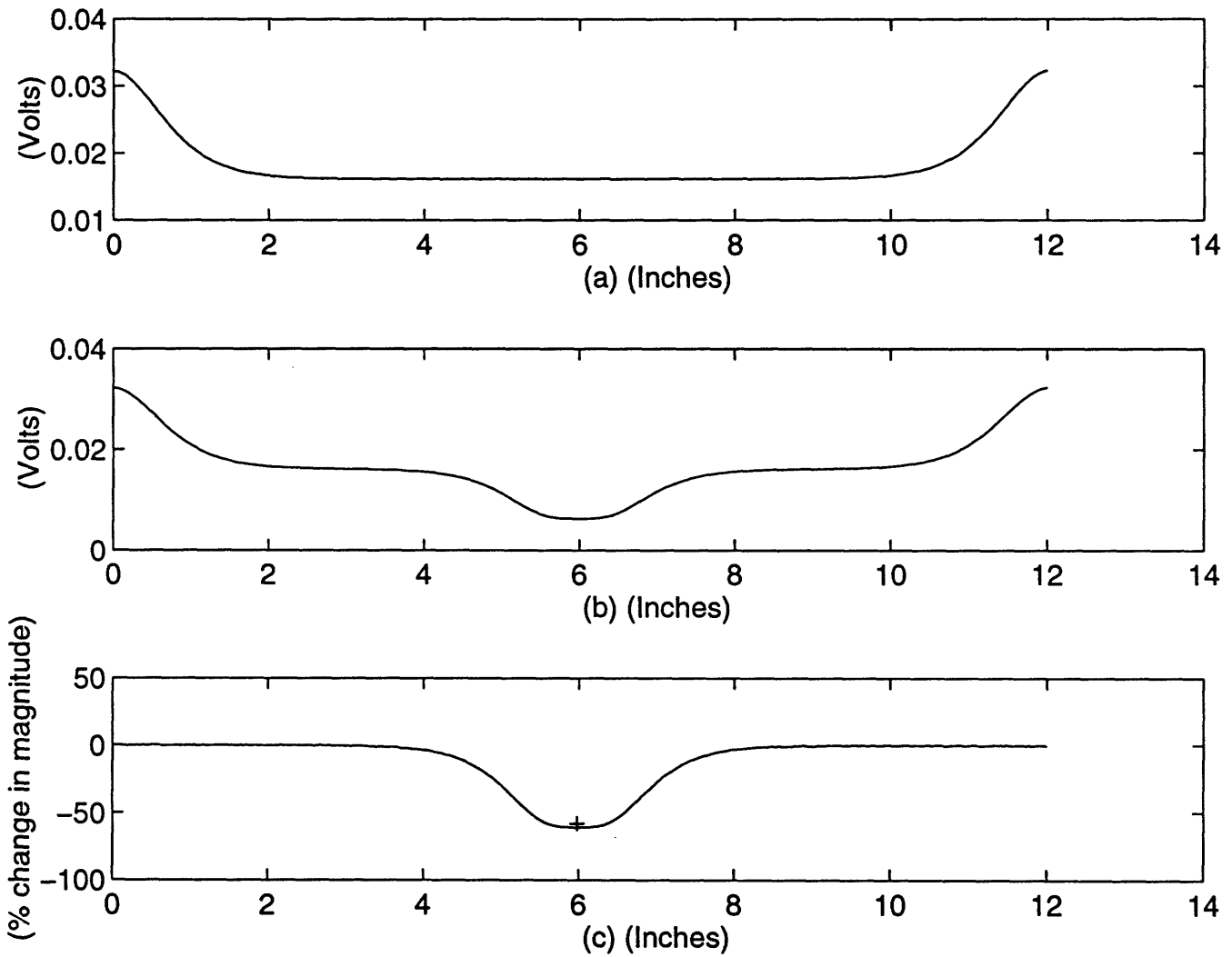
Figure 2.5: Two absorbers placed 2 cm apart and 1.5 cm away from the detector edge: computer simulation result (_) and experimental peak and dip locations (+); output potential due to nominal absorption (a), output potential with perturbation in absorption (b), and percent change in magnitude from the nominal to the perturbed case (c).
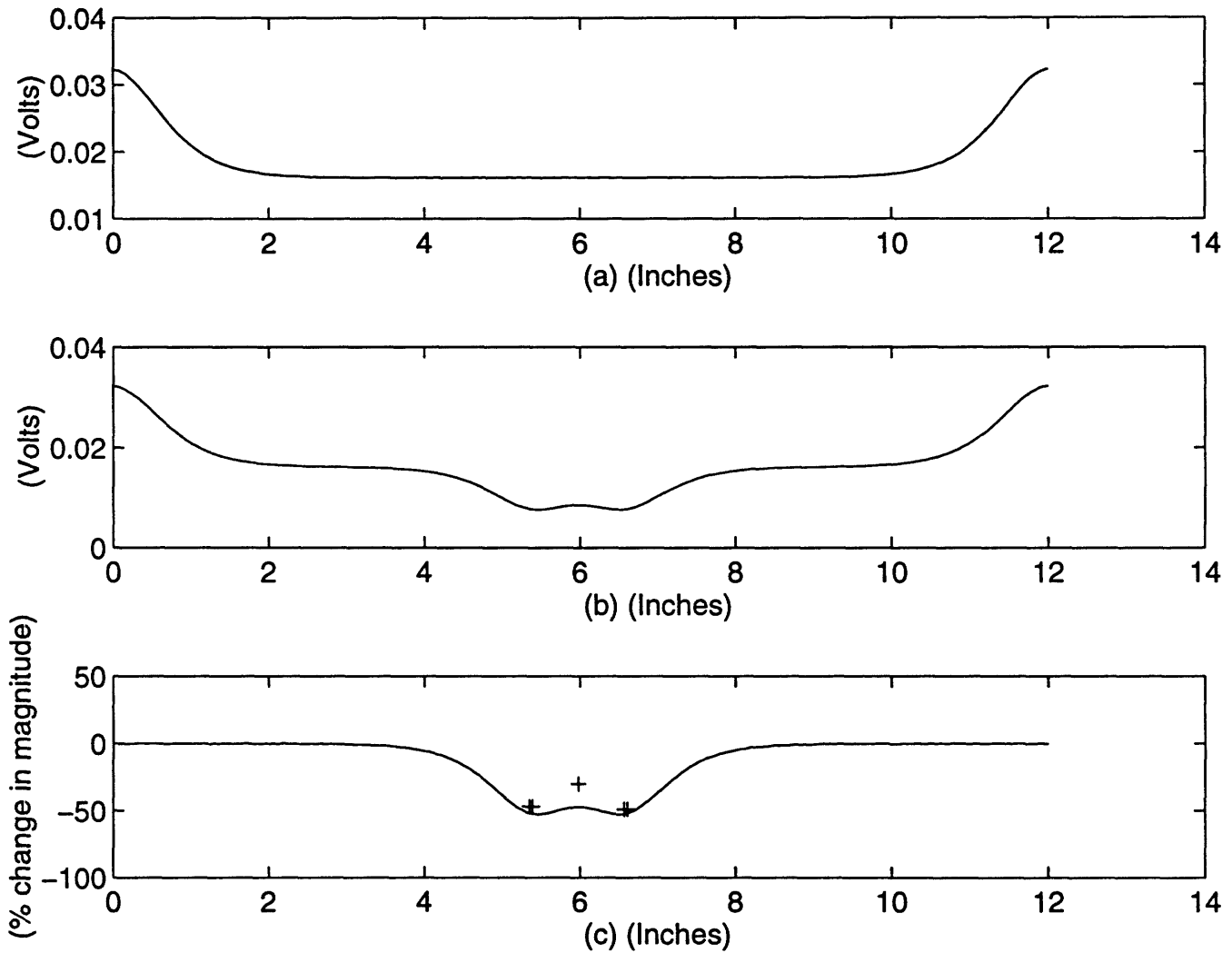
Figure 2.6: Two absorbers placed 3 cm apart and 1.5 cm away from the detector edge: computer simulation result (_) and experimental peak and dip locations (+); output potential due to nominal absorption (a), output potential with perturbation in absorption (b), and percent change in magnitude from the nominal to the perturbed case (c).

seven and forty-nine percent and a relative maximum peak between them at about thirty percent. Again, the simulation duplicated the experimental results well.

One problem with these simulations is that the outputs are not as strongly attenuated as we would expect, according to the number of scattering lengths which are traversed in the two depths of simulated tissue [20].

We would expect the nominal output potentials in the center of the width of the simulated tank to differ for the two different tank depths by $e^{-(\text{number of space constants in one inch})}$. Since the transport cross section for the Intralipid-10%™ is 0.392 mm^{-1}, the scattering length is about 2.5 mm, and there are about ten scattering lengths in an inch. Then, the difference between the two measurements should be by a factor of e^{-10} or about 1/22,000. Instead, there is only a factor of five difference between the two nominal output potentials. The model does not decay exponentially with a space constant equal to the inverse of the transport cross section.

We attribute this problem to the fact that the absorption of Intralipid-10%™ is negligible [43, p. 2293]. We tried the same simulations with parameters which correspond to breast tissue, and this case involves an absorption coefficient which is high enough to produce nearly the expected attenuation. With these values, the transport cross section is 0.2578 mm^{-1}, and the scattering length is about 4 mm, and so there are about 6.55 scattering lengths in an inch. The attenuation should be about $e^{-6.55}$, or about 1/700. The results of this investigative simulation are shown in Figures 2.7, 2.8, 2.9, and 2.10. Their experimental configurations correspond to those of Figures 2.3, 2.4, 2.5, and 2.6, respectively. The nominal output potential in the middle of the 1" tank is about 2.39e-4 Volts, and in the middle of the 2" tank it is about 4.23e-7 Volts. The difference between the two is a factor of 565. This is much closer to 700 than five is to 22,000. When the absorption coefficient is nearly zero (as in the case of the simulations which model Intralipid-10%™), the conductances to ground are also nearly zero. We expect that this is the reason for the low

29
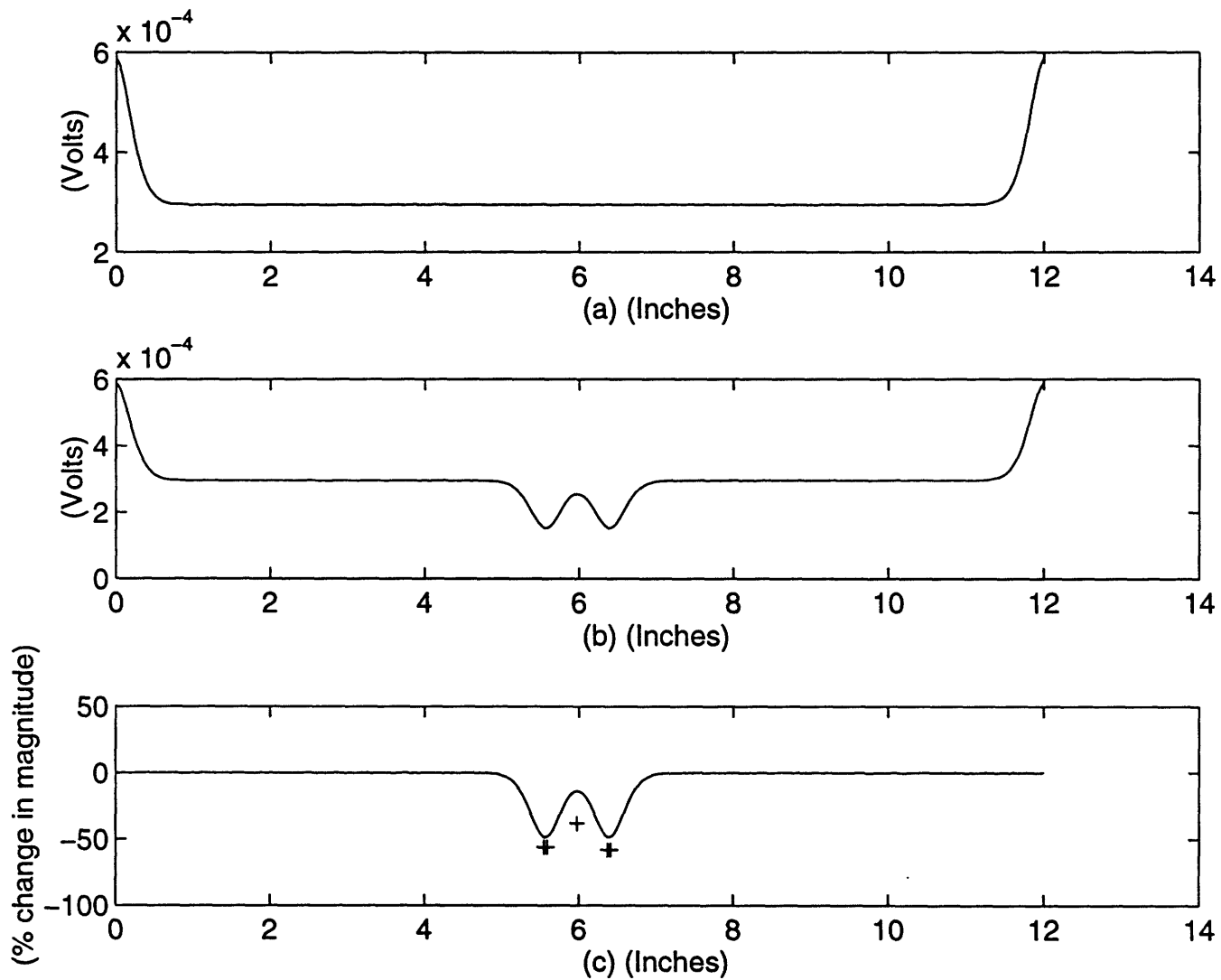
Figure 2.7: Two absorbers placed 2 cm apart and 1.2 cm away from the detector edge: computer simulation result (_) and experimental peak and dip locations (+); output potential due to nominal absorption (a), output potential with perturbation in absorption (b), and percent change in magnitude from the nominal to the perturbed case (c). Parameters correspond to breast tissue.
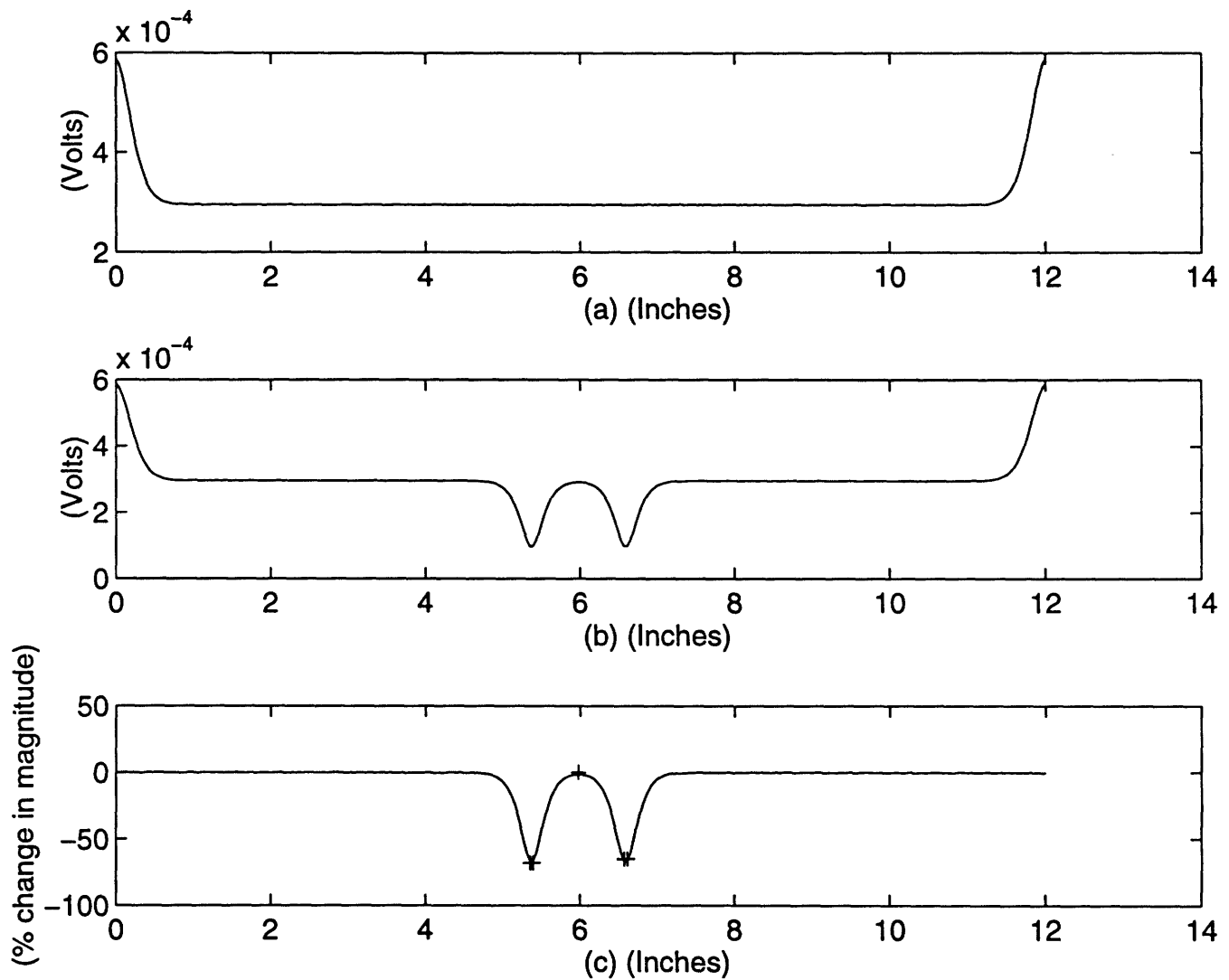
Figure 2.8: Two absorbers placed 3 cm apart and 2.0 cm away from the detector edge: computer simulation result (_) and experimental peak and dip locations (+); output potential due to nominal absorption (a), output potential with perturbation in absorption (b), and percent change in magnitude from the nominal to the perturbed case (c). Parameters correspond to breast tissue.
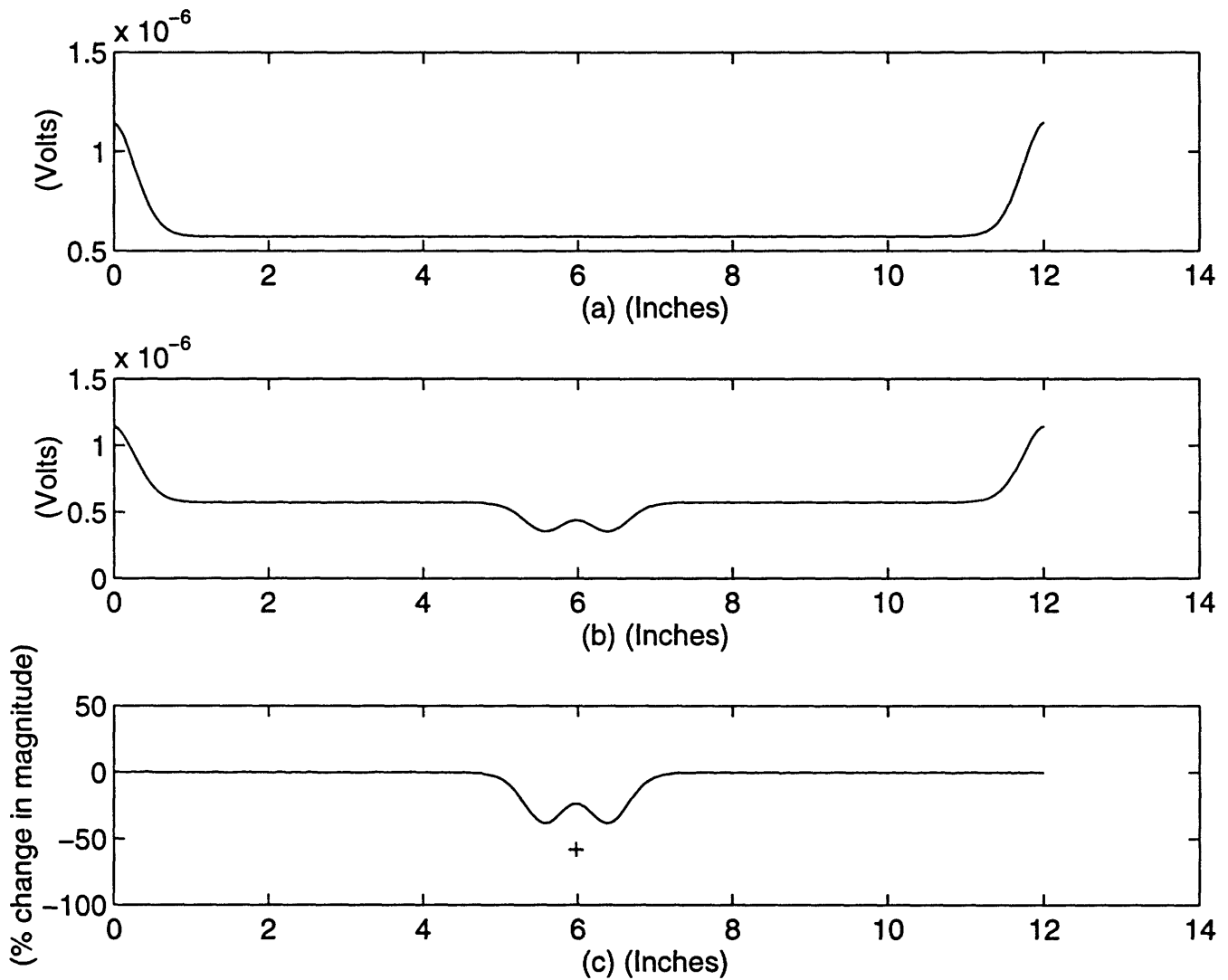
Figure 2.9: Two absorbers placed 2 cm apart and 1.5 cm away from the detector edge: computer simulation result (_) and experimental peak and dip locations (+); output potential due to nominal absorption (a), output potential with perturbation in absorption (b), and percent change in magnitude from the nominal to the perturbed case (c). Parameters correspond to breast tissue.
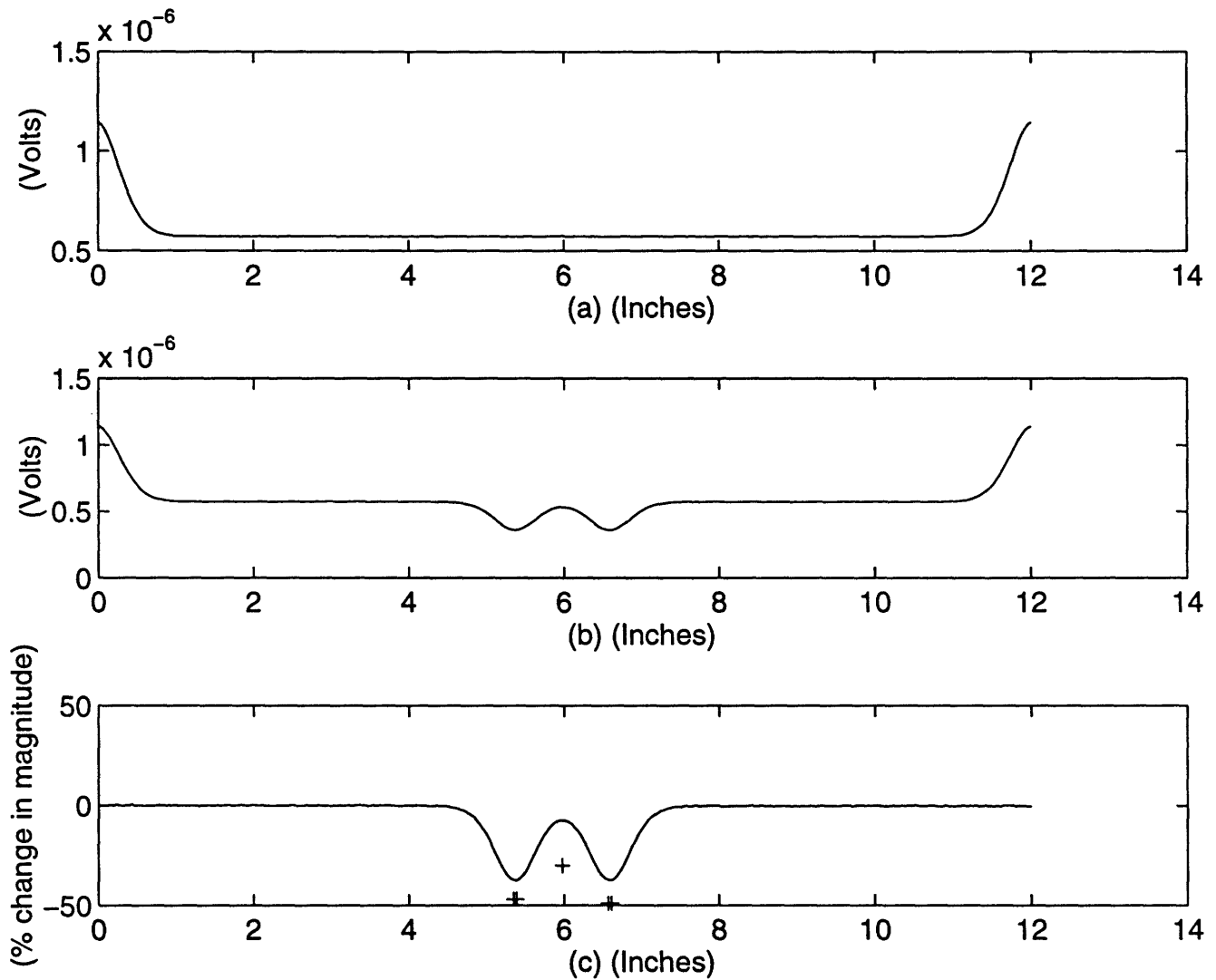
Figure 2.10: Two absorbers placed 3 cm apart and 1.5 cm away from the detector edge: computer simulation result (_) and experimental peak and dip locations (+); output potential due to nominal absorption (a), output potential with perturbation in absorption (b), and percent change in magnitude from the nominal to the perturbed case (c). Parameters correspond to breast tissue.

attenuation in the first set of simulations.

This series of experiments gives a good amount of initial confidence in this resistive grid model of the diffusion approximation. The experimental data was only communicated by means of peaks and dips in magnitude, so that a very precise comparison is not possible.

3. The Discretized Forward and Inverse Problems in Two Dimensions

First let us get a solid picture of the discrete network topology which was introduced informally in Section 2.2. The result is a simple, two-dimensional resistive grid upon which the problem can be generally defined. Recall that the model consists of a two-dimensional lattice of nodes which are connected by resistors, and each node is connected to ground through an additional resistor. A slightly more comprehensive model would extend this grid into three dimensions, and may move into the time-dependent regime.

If we let H be the number of nodes in the height of the two-dimensional grid, and let W be the number of nodes in the width of the grid, then we can implement a node-numbering sequence as depicted in Figure 3.1 below.
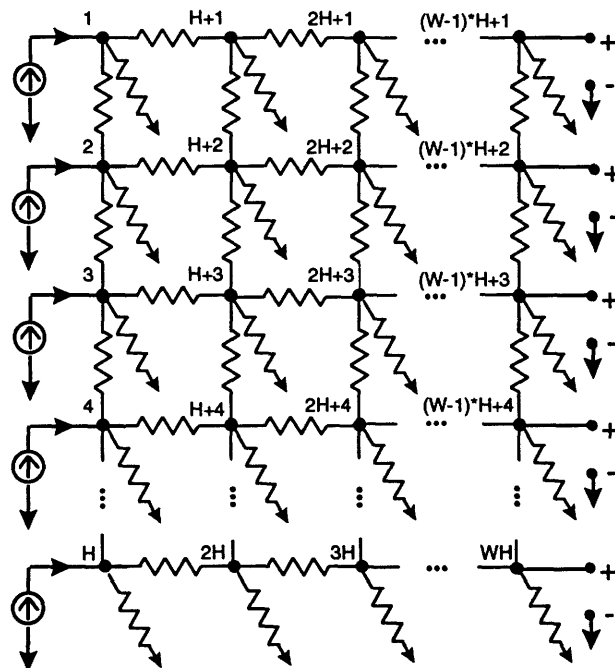
Figure 3.1: Resistive Grid

We will refer to nodes 1 through H as the *input* nodes, those on the left edge of the grid, and to nodes (W-1)*H+1 through W*H as the *output* nodes, which are located on the right edge of the grid. The light input which is incident

upon the left side of the grid is modeled as current; the nodes on the right side of the grid are analogous to the light output intensities which we would measure experimentally, and in the simulation we compute the voltage potential at those locations.

3.1 General Mathematical Formulation of the Forward Problem

We consider the conductance matrix, $\mathbf{G}$, to be a sum, $\mathbf{G} = \mathbf{G}_h + \mathbf{G}_v$, the conductance due to the horizontal resistors (those between neighboring nodes) plus the conductance due to the vertical resistors (those from each node to ground). We have a good understanding of what $\mathbf{G}$ is for normal, healthy tissue, and we refer to this general case as $\mathbf{G}_{nom}$, the nominal conductance matrix. It is related to the potential, $\mathbf{v}$, and the current, $\mathbf{i}$, by the following equation:

$$\mathbf{Gv} = \mathbf{i}. \qquad (3.1)$$

In cancerous tissue, we say that there is a non-negatively-valued perturbation, $\delta\mathbf{G}$, from the nominal conductance matrix, so that we now have a conductance matrix which is equal to:

$$\mathbf{G} = \mathbf{G}_{nom} + \delta\mathbf{G}.$$

We can define a *forward problem* which consists of determining a vector $\mathbf{v}_{nom}$ of node voltages, given the conductance matrix, $\mathbf{G}_{nom}$, and the current input to each node, $\mathbf{i}$, such that:

$$\mathbf{G}_{nom}\mathbf{v}_{nom} = \mathbf{i}, \qquad (3.2)$$

or, with the perturbation, such that:

$$(\mathbf{G}_{nom} + \delta\mathbf{G})(\mathbf{v}_{nom} + \delta\mathbf{v}) = \mathbf{i}. \qquad (3.3)$$

In the *experimental* forward problem, we are unable to measure the potential on the interior of the model. In the *simulated* forward problem, we may determine all of $\mathbf{v}$ *computationally*, for arbitrary geometries. Also, in the *experimental* forward problem, we may only inject current along the boundary;

and specifically, only on regions of the boundary which are considered part of the input. The current everywhere else is equal to zero.

In our numbering scheme, this means that we can only measure the output potentials at the *last* H nodes, and that we can only inject current at the *first* H nodes. Since we can only measure output potentials from node [(W-1)*H+1] to node [W*H], we have only H measurements and thus H equations for each single-node current injection experiment. If we could measure all of the potential values along the grid, we would have W*H equations for each single-node current injection experiment. Since there are H injection nodes, we have H^2 equations overall.

What kind of a matrix are we dealing with here? Because **G** is the conductance matrix in a resistive circuit equation, it exhibits reciprocity and is therefore symmetric.[5] Another result of its being the conductance matrix in a resistive circuit equation is that **G** is an M-matrix.[6] As long as there is a nonzero conductance to ground at every node, **G** is *strictly* diagonally dominant; otherwise, it is *weakly* diagonally dominant. **G** has a sparse, Toeplitz-like structure due to the second spatial derivative in the corresponding diffusion equation: grid neighbors which are symmetric about a node, and adjacent to it, are represented at equal distances to the right and left of an element on the main diagonal in **G**. The physical cause of this banded structure is the isotropic scattering.

As an example of the numerical structure of the conductance matrix, consider a single node, k, of a resistive grid, such as one of the nodes in Figure 3.1. Isotropic scattering dictates that photons propagate radially outward from their point of incidence, which we take to be grid node k. The four nearest

---

[5] If we have any two unique electrical events on the grid and the corresponding current and potential vectors for each, reciprocity implies that the inner product of one current vector and the other potential vector is equal to the inner product of the remaining two vectors. The network is reciprocal since it is constructed from linear 2-terminal resistors, and reciprocity implies symmetry of the conductance matrix [22, pp. 102-103].

[6] By definition, **G** then has non-positive off-diagonal entries, and its inverse is nonnegative. Because we know that it is symmetric, the fact that it is an M-matrix also implies that it is positive definite, and all the entries in its inverse are positive [29, pp. 44, 93].

neighbors are at nodes k-1, k+1, k-H, and k+H. For each k, the node relationships between node k and these neighboring locations are represented in the conductance matrix by entries one band to the right and left of the main diagonal, and H bands to the right and left of the main diagonal. For a grid like the one in Figure 3.1 which is four nodes tall and three nodes wide, if each resistor has a resistance of 1 Ohm, then a sample conductance matrix (in mho) is:

$$
G = \begin{bmatrix}
3 & -1 & 0 & 0 & -1 & 0 & 0 & 0 & 0 & 0 & 0 & 0 \\
-1 & 4 & -1 & 0 & 0 & -1 & 0 & 0 & 0 & 0 & 0 & 0 \\
0 & -1 & 4 & -1 & 0 & 0 & -1 & 0 & 0 & 0 & 0 & 0 \\
0 & 0 & -1 & 3 & 0 & 0 & 0 & -1 & 0 & 0 & 0 & 0 \\
-1 & 0 & 0 & 0 & 4 & -1 & 0 & 0 & -1 & 0 & 0 & 0 \\
0 & -1 & 0 & 0 & -1 & 5 & -1 & 0 & 0 & -1 & 0 & 0 \\
0 & 0 & -1 & 0 & 0 & -1 & 5 & -1 & 0 & 0 & -1 & 0 \\
0 & 0 & 0 & -1 & 0 & 0 & -1 & 4 & 0 & 0 & 0 & -1 \\
0 & 0 & 0 & 0 & -1 & 0 & 0 & 0 & 3 & -1 & 0 & 0 \\
0 & 0 & 0 & 0 & 0 & -1 & 0 & 0 & -1 & 4 & -1 & 0 \\
0 & 0 & 0 & 0 & 0 & 0 & -1 & 0 & 0 & -1 & 4 & -1 \\
0 & 0 & 0 & 0 & 0 & 0 & 0 & -1 & 0 & 0 & -1 & 3
\end{bmatrix}.
$$

The matrix is *nearly* Toeplitz along its off-diagonals, but there are notches (zeros instead of nonzero values) at some locations in the band which is one diagonal away from the main diagonal. This results from the spatial discontinuities at the top and bottom edges of the grid, where numerically-sequential nodes (as they are indexed in Figure 3.1) are not neighbors, as a single-valued band in **G** would have to imply.

3.2 General Mathematical Formulation of the Nonlinear Inverse Problem

We have defined a generalized *forward problem*; we can similarly define an *inverse problem* in which we would like to find the perturbation δG for which a *set* of measured output vectors $(v^d_{nom,m} + \delta v^d_m)$ (the subscript 'm' represents the

nodes which we are able to measure, and the superscript 'd' represents the nodes at which we can drive with current) agree most closely with their corresponding entries in the computed set of vector expressions:

$$\left[\mathbf{G}_{nom} + \delta\mathbf{G} \right]^{-1} \mathbf{i}^d.$$

This expression comes from rearranging terms to isolate (v+ δv) in Equation 3.2. The inverse problem is a nonlinear one because the matrix inverse is a nonlinear expression in $\mathbf{G}_{nom} + \delta\mathbf{G}$.

3.3 The Forward Problem Specific to this Research

This research effort focuses on the two-dimensional slice of resistive grid elements which is H nodes high and W nodes wide, as in Figure 3.1. We further simplify the problem by assuming that only the vertical conductances, those we attribute to the absorption coefficient, are perturbed in the conductance matrix for cancerous tissue, where $\mathbf{G} = \mathbf{G}_{nom} + \delta\mathbf{G}$.[7] The elements of δG are solely along the diagonal of G, so that we may write the perturbed conductance matrix G as:

$$\mathbf{G} = [\,\mathbf{G}_{nom} + \text{diag}(\mathbf{x})], \qquad (3.4)$$

where x is the vector of perturbations in conductance for which we would like to solve, and the 'diag' function maps a vector into a diagonal matrix. We define:

$$\mathbf{R}(\mathbf{x}) = \mathbf{G}^{-1}(\mathbf{x}). \qquad (3.5)$$

The forward problem is then defined by solving for v due to each of the many current vectors, i, such that:

$$\mathbf{v} = \mathbf{R}(\mathbf{x})\,\mathbf{i}. \qquad (3.6)$$

---

[7] This assumption does not agree with the derivation in Chapter 1, but we will assume for now that it is a close approximation to the actual perturbation.

3.4 The Nonlinear Inverse Problem Specific to this Research

In this research problem, we are more directly concerned with the *inverse problem* of finding **G** given *many* potential vectors, **v**, which are the results of *many* different current injections, **i**. To measure the agreement between the output potentials which we can measure and the corresponding potentials calculated from our guess at the perturbation in conductance, we use the squared Euclidean norm, which in this case is:

$$\Phi(\mathbf{x}) = \sum_{d=1}^{H} \sum_{m=H(W-1)+1}^{HW} \left[(\mathbf{R}(\mathbf{x})\mathbf{i})_m^d - \mathbf{v}_{meas,m}^d \right]^2 . \qquad (3.7)$$

The purpose of the inverse problem is to find the global minimum of this squared norm. This is difficult to do, because it is a nonlinear function. My approach at the inverse problem consists of finding a local stationary point of $\Phi(\mathbf{x})$ which may or may not be its global minimum.

Note that the first term in the brackets of Equation 3.7 is actually the bottom left HxH block of the inverse of the conductance matrix. $\mathbf{R}(\mathbf{x})$ is the entire inverse of **G**, but the subscripts 'd' and 'm' pick out its first H columns and last H rows, respectively. Being able to inject current only at the first H nodes means that only the first H entries of **i** can ever be nonzero, so only the first H columns of $\mathbf{R}(\mathbf{x})$ will be preserved in the product. Also, the subscript 'm' implies that we are only considering the nodes along the output in **v**, so we neglect all but the last H rows of $\mathbf{R}(\mathbf{x})\mathbf{i}^d$. And thus, we are left with the bottom HxH block of $\mathbf{R}(\mathbf{x})$ in Equation 3.7.

The forward problem is known to be very insensitive since a large perturbation in absorption will result in a very small change in measured output potential. Therefore, when we observe a very small change in output potential (such as that due to measurement noise), we tend to expect that it was caused by a large perturbation in absorption. The inverse problem is therefore challenging and misleading and is referred to as being highly *sensitive* due to the *insensitive* forward problem.

The forward problem is also complicated because the **G** matrix, although nonsingular, is computationally prohibitive to invert due to its large size. Even if we could easily invert **G**, the amount of information we can learn about the problem due to a single current injection and the corresponding set of output potentials is very low.

We approach the solution to the inverse problem by assembling a set of equations due to many injection sites and their corresponding output potentials, in an effort to compensate for both the lack of information in solving the forward problem for the result of a single current injection system and the sensitivity to measurement noise. We hope that taking many measurements will make it more clear what is noise and what is a perturbation-induced change in output potential.

It has been suggested that increasing the number of injection sites, and therefore different i's for which we solve the forward problem, may make the inverse problem more well-determined in the continuous regime; in the discrete context of this problem, we can analogously expect an improvement in the conditioning of the problem [24, 41].[8]

---

[8] A continuous partial differential equation may be characterized as 'well-determined', but in our discrete version of the problem, this characteristic depends on the fineness of the discretization and can be measured with the condition number of the problem [41]. What happens is that each entry of the solution to a linear equation is proportional to the inverse of its corresponding singular value [44, p. 55]. As the grid spacing becomes finer and therefore the number of unknowns becomes very large, the number of singular values exceeds the number of independent equationsin the problem so that some of the singular values go to zero, so that thecorresponding solutions blow up [44, p. 55]. The condition number is the ratio of largest to smallest singular values, so that when the smallest singular value is near zero, the condition number will be very large and we then say that the linear operator is ill-conditioned [8, Section 2.7.2].

It should be much easier to solve the forward problem several times than to invert the conductance matrix in solving the nonlinear problem. We therefore look for ways to use the forward problem to solve the inverse problem, such as by using a modified version of Newton's Method with a quadratic cost function, a variation on a suggestion of Dr. Arridge. This topic and related issues will be discussed with references in Chapter 5.

4. Linear Formulation of the Inverse Problem

A popular approach to simplifying the nonlinear inverse problem involves linearizing about the nominal conductance, G_{nom}, so that a system of equations can be analyzed in terms of a perturbation of the conductance from the nominal values [24]. As stated in Section 3.3, we assume that only the vertical conductances, those along the diagonal of G, are perturbed.

We have defined v^d as the solution to the forward problem when i is zero for all entries except the dth, which is equal to 1 Ampere. Similarly, e_m is defined as the solution to the forward problem when i is zero for all entries except the $((W-1)*H + m)^{th}$, one of the nodes along the output, which is also equal to 1 Ampere. Given the forward problem, if we perturb G by δG such that:

$$(G + \delta G)(v^d + \delta v^d) = i^d,$$

resulting in:

$$Gv^d + G\delta v^d + \delta Gv^d + \delta G\delta v^d = i^d, \qquad (4.1)$$

we can subtract the equality $Gv^d = i^d$ from this product. We can further subtract the nonlinear term $\delta G\delta v^d$, because the perturbation δG (and therefore the change in output potential it induces, δv^d) are small enough when compared with the other terms in the equation that their second-order product is practically negligible. These subtractions reduce the expression to:

$$G\delta v^d + \delta Gv^d = 0. \qquad (4.2)$$

How can we solve for δG? We know all of G, the nominal conductance matrix, and all of v^d, the response to the nominal G when the circuit is injected with 1 Ampere of current at node d. The fact that we can only measure the last H values of δv^d suggests that we should eliminate the unknowns from the system in Equation 4.2 [20]. In the paragraphs below we do just that, and the result is a linear expression for δG which relies on the Jacobian matrix.

43

We first begin by separating the components of the first term in Equation 4.2 into two parts. Let $\mathbf{G}_{interior}$ be the first $(W-1)*H$ columns of $\mathbf{G}$ (corresponding to the input nodes and interior nodes of the resistive grid model), while $\mathbf{G}_{meas}$ is the last H columns of $\mathbf{G}$ (corresponding to the output nodes). Similarly, let $\delta \mathbf{v}_{interior}^{d}$ be the first $(W-1)*H$ entries of $\delta \mathbf{v}^{d}$ and let $\delta \mathbf{v}_{meas}^{d}$ be the last H entries. The new form of Equation 4.2 is then:

$$\mathbf{G}_{interior}\,\delta \mathbf{v}_{interior}^{d} + \mathbf{G}_{meas}\,\delta \mathbf{v}_{meas}^{d} + \delta \mathbf{G} \mathbf{v}^{d} = 0. \qquad (4.3)$$

To follow the suggestion from the paragraph above and eliminate unknowns from Equation 4.3, we multiply the entire system by $\mathbf{e}_{m}^{\mathsf{T}}$, which is defined at the beginning of Chapter 4. This gives:

$$\mathbf{e}_{m}^{\mathsf{T}}\,(\mathbf{G}_{interior}\,\delta \mathbf{v}_{interior}^{d} + \mathbf{G}_{meas}\,\delta \mathbf{v}_{meas}^{d} + \delta \mathbf{G}\,\mathbf{v}^{d}) = 0. \qquad (4.4)$$

Now, $\mathbf{e}_{m}$ is orthogonal to all rows of $\mathbf{G}$ (and therefore all of the columns, since $\mathbf{G}$ is symmetric), except for the $((W-1)*H+m)^{th}$, since $\mathbf{G}\mathbf{e}_{m} = \mathbf{i}_{m}$ where all of $\mathbf{i}$ is zero except for the $((W-1)*H+m)^{th}$ element.[9] This eliminates the first term in Equation 4.4 due to the definition of $\mathbf{G}_{interior}$. This also reduces the second term in Equation 4.4 to 1 Ampere times $\delta \mathbf{v}_{meas,m}^{d}$, the change in measured output potential which is observed at node $((W-1)*H+m)$ due to a current injection at node d. Because $\delta \mathbf{G}$ is a diagonal matrix, with appropriate multiplying of terms, we can use its vector definition, $\mathbf{x}$, from Section 3.3, and rearrange what remains of Equation 4.4 to:

$$(\mathbf{e}_{m}.^{*}\mathbf{v}^{d})^{\mathsf{T}}\mathbf{x} = -\,\delta \mathbf{v}_{meas,m}^{d}, \quad 1 \leq m \leq H \text{ and } 1 \leq d \leq H. \qquad (4.5)$$

The '.*' represents term-by-term multiplication, so that the '.*' product of two vectors remains a vector. Assembling this equation for all m's and all d's will result in the coefficient of $\mathbf{x}$ being equal to the Jacobian of the output potentials

---

[9] This is due to Equation 3.1.

44

with respect to the vertical conductances.[10] This constitutes our linearization of the nonlinear inverse problem.

We are able to solve for **x** in Equation 4.5 in a region where the linear approximation is appropriate. In order to avoid overshooting the solution, this may require a scaling of the linear result before considering it to be an update to the previous guess at the nonlinear solution. For example, we can calculate an initial guess, **x**, and scale it by half until it shows an improvement from the result of the last iteration. This procedure is discussed in more detail in Sections 5.2 and 5.3.

4.1 Limitations of the Linear Formulation

The most obvious problem with linearization is the loss of valuable information due to the removal of the second-order term. From the part of the equation which states:

$$G\delta v^d + \delta G v^d + \delta G \delta v^d = 0$$

in the forward problem, we have linearized to arrive at Equation 4.5. This equation neglects the $\delta G \delta v^d$ term, which is small compared with the other terms in the problem. The change in conductance, δG, is a positive one since a tumor has a higher absorption than normal tissue. The resultant higher conductance decreases the output potential by bringing more current down to ground on the interior of the tissue model, and leaving less to be measured at the output, so that δv^d is negative for nonzero δG. A linear approximation to this nonlinear problem predicts a decreasing measured output potential with increasing δG. The decrease in output potential extends through zero into negative potentials, which is physically impossible. The exact model of changing output potential

---

[10] The [i,j] entry of the Jacobian matrix of the vector function, **g**, at a point **x**, where **g**: $\mathfrak{R}^N \to \mathfrak{R}^M$, is defined as: $[\mathbf{J}(\mathbf{g}(\mathbf{x}))]_{i,j} = \dfrac{\delta g_i}{\delta x_j}(\mathbf{x})$, $1 \leq i \leq M$ and $1 \leq j \leq N$.

45

with respect to increasing δG asymptotically approaches some non-negative value, and is made more positive and less linear by the $\delta G \delta v^d$ term.

We can verify this asymptotic behavior by taking the derivative twice with respect to G, in a matrix-vector version of the circuit equation [20]. The first derivative of Equation 3.1 is:

$$\frac{\delta}{\delta g_{k,k}}(Gv - i) = \frac{\delta G}{\delta g_{k,k}}v + G\frac{\delta v}{\delta g_{k,k}} = 0,$$

where $g_{k,k}$ is the kth entry of G. Rearranging terms, and using the fact that:

$$\left[\frac{\delta G}{\delta g_{k,k}}\right]_{i,j} = \delta_{i,k}\delta_{j,k},$$

the result is:

$$\begin{pmatrix} 0 \\ v_k \\ 0 \end{pmatrix} + G\frac{\delta v}{\delta g_{k,k}} = 0.$$

The derivative of v with respect to $g_{k,k}$ is then:

$$\frac{\delta v}{\delta g_{k,k}} = -R\begin{pmatrix} 0 \\ v_k \\ 0 \end{pmatrix},$$

where R is the inverse of G. This derivative is entirely non-positive since voltage potentials must always be positive or zero, and every entry of R is non-negative, by definition, since G is an M-matrix [29, p. 93].[11]

The second derivative of the circuit equations is:

$$\left[\begin{pmatrix} 0 \\ \frac{\delta v_k}{\delta g_{k,k}} \\ 0 \end{pmatrix} + \frac{\delta G}{\delta g_{k,k}}\right]\frac{\delta v}{\delta g_{k,k}} + G\frac{\delta^2 v}{\delta g_{k,k}^2} = 0.$$

Rearranging terms we get:

---

[11] In addition, this definition implies that G is nonsingular, square, and that each off-diagonal element is negative or zero [20].

$$\frac{\delta^2 \mathbf{v}}{\delta g_{k,k}^2} = -\mathbf{R}\begin{pmatrix} \mathbf{0} \\ \frac{\delta \mathbf{v}_k}{\delta g_{k,k}} \\ \mathbf{0} \end{pmatrix} - \begin{pmatrix} 0 & \mathbf{R}_{:k} & 0 \end{pmatrix}\begin{pmatrix} \frac{\delta \mathbf{v}}{\delta g_{k,k}} \end{pmatrix}, \qquad (4.6)$$

where the notation $\mathbf{R}_{:k}$ represents all the entries in column k of the $\mathbf{R}$ matrix. Because there are entirely negative terms (the -$\mathbf{R}$'s) multiplying the first derivatives in the right hand side of Equation 4.6 and because the first derivative is entirely negative or zero, this second derivative of $\mathbf{v}$ with respect to $\mathbf{G}$ is non-negative. This analysis demonstrates that, although $\mathbf{v}$ decreases with increasing $\mathbf{G}$ (the first derivative of $\mathbf{v}$ with respect to $\mathbf{G}$ is negative), it is not linear since the rate of change of $\mathbf{v}$ with respect to $g_{k,k}$ is increasing (the second derivative of $\mathbf{v}$ with respect to $\mathbf{G}$ is non-negative and the potentials therefore approach either a minimum or a saddle point). Since we know the potential has to be non-negative, and because of this increasing rate of change indicated by the second derivative, we know that $\mathbf{v}$ must asymptotically approach zero or some positive value as the $g_{k,k}$'s approach infinity. A linear approximation overlooks this asymptotic behavior, but is a good first-order estimate along small sections of the nonlinear cost function, $\Phi(\mathbf{x})$, in Equation 3.7.

Another problem with the linear approximation is that some changes in output potential are so small that they go unnoticed. Furthermore, perturbations from the nominal conductance may produce a change in potential which is exactly equal to zero if $\delta \mathbf{G}$ is in the nullspace of $(\mathbf{e}_m.^*\mathbf{v}^d)^T$. This may allow small errors to grow in an iterative, incrementally linear, guess at the solution. We discuss this circumstance further below.

To demonstrate the case where a change in conductance might not produce a change in the output potential, consider again the elliptical source and detector dependence (recall Figure 2.1 and Equation 2.10). If a collection of grid locations each have the same [distance to source plus distance to detector], they will have an equal influence on the output potential they induce. Therefore, if we have a set of perturbations in conductance along one of these ellipses, and

47

the accumulated perturbation along the ellipse is equal to zero, then together they have a zero contribution to the overall output potential. We hypothesize that perturbations in conductance along ellipses of constant influence which together sum to zero will yield a change in output potential which is very close to zero, so that these perturbations are very close to being in the nullspace of the Jacobian. This should be the case with a perturbation in absorption which is symmetric across the width of the grid, as in Figure 4.1 (a). Its induced output intensity is on the order of 10^{-18}, as in Figure 4.1 (d), whereas the output intensity due to the perturbations in absorption which are not symmetric about the center of the width of the grid, as in Figure 4.1 (b) and (c), produce output intensities on the order of 10^{-3}, as in Figures 4.1 (e) and (f).

There are limitations involved with the linear formulation of the problem, but it is generally helpful in stepping toward a possible solution to the nonlinear problem. This is especially true since Equation 4.5 contains the Jacobian of the output potentials with respect to the conductance to ground at each node. This Jacobian is much easier than the analytical one to compute.

4.2 Rank Deficiency and Least Squares

In Section 3.4 we introduce the idea of bringing more information to the problem by assembling many more equations than there are unknowns. This type of formulation historically suggests a solution based on the least squares minimization of some cost function. In our case, the cost function is $\Phi(\mathbf{x})$.

Because this is a *nonlinear* least squares problem, we attempt to solve it iteratively, solving a linear least squares problem at each iteration. Starting with the initial guess that $\mathbf{x} = 0$ (corresponding to the nominal conductance), our solution algorithm steps linearly in $\mathbf{x}$ toward a stationary point of $\Phi(\mathbf{x})$. The algorithm is developed in more detail in Section 5.2.
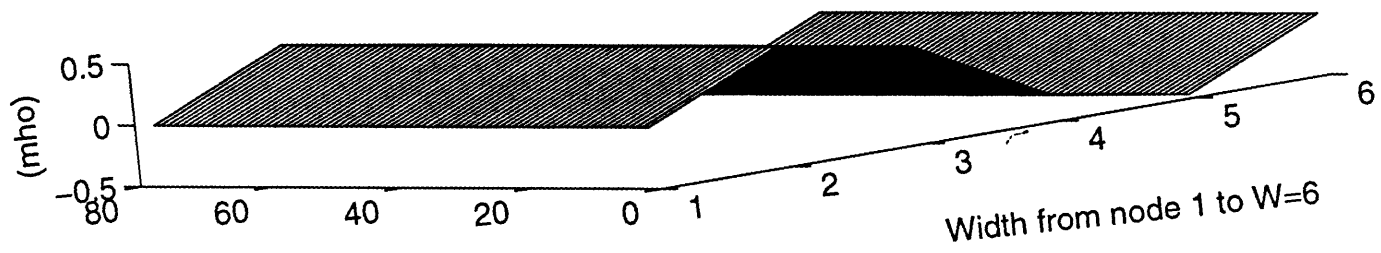
a) Height from node 1 to H=77
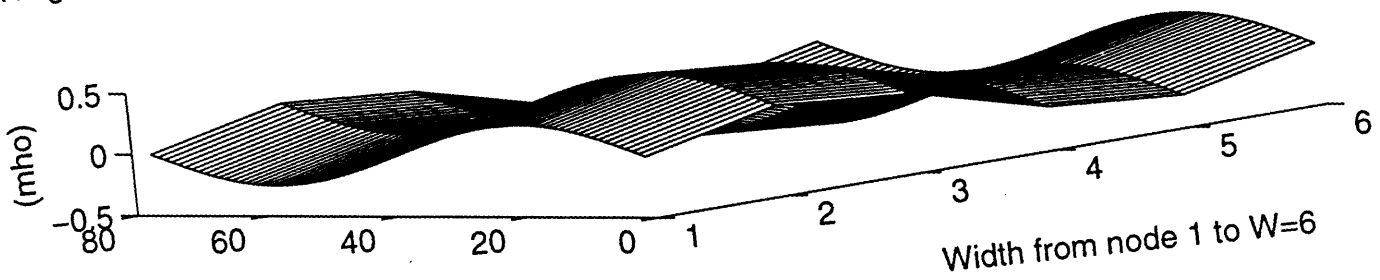
b) Height from node 1 to H=77
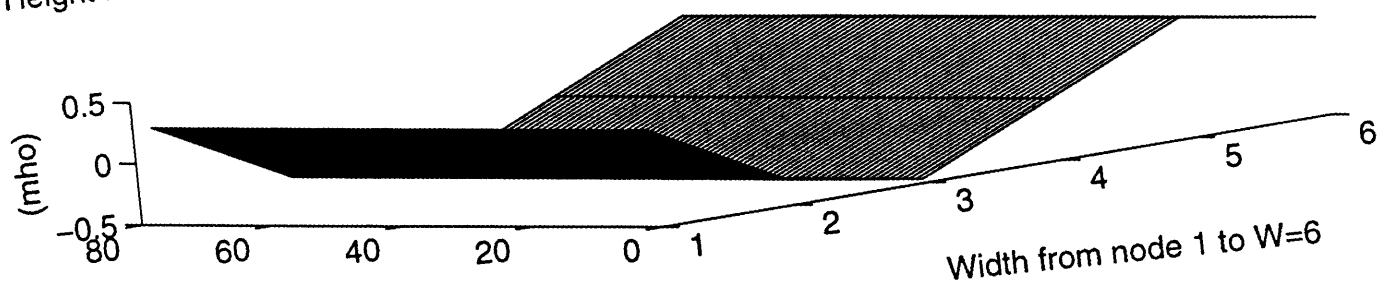
c) Height from node 1 to H=77

Figure 4.1: Perturbations from the nominal absorption of 0.8016 mho which are: sinusoidal and symmetric about the depth center of the grid (a); sinusoidal and symmetric about the center of the depth of the grid plus sinusoidal and symmetric about the center of the height of the grid, divided by two (b); sinusoidal and varying along the depth of the grid, shifted to avoid symmetry (c).

49

$\times 10^{-18}$

(Volts)

2

0

-2

80   60   40   20   0   0   20   40   60   80

H=77 equations

(d) H=77 output potentials

$\times 10^{-3}$

(Volts)

2

0

-2

80   60   40   20   0   0   20   40   60   80

H=77 equations

(e) H=77 output potentials

$\times 10^{-3}$

(Volts)

2

1

0

80   60   40   20   0   0   20   40   60   80

H=77 equations
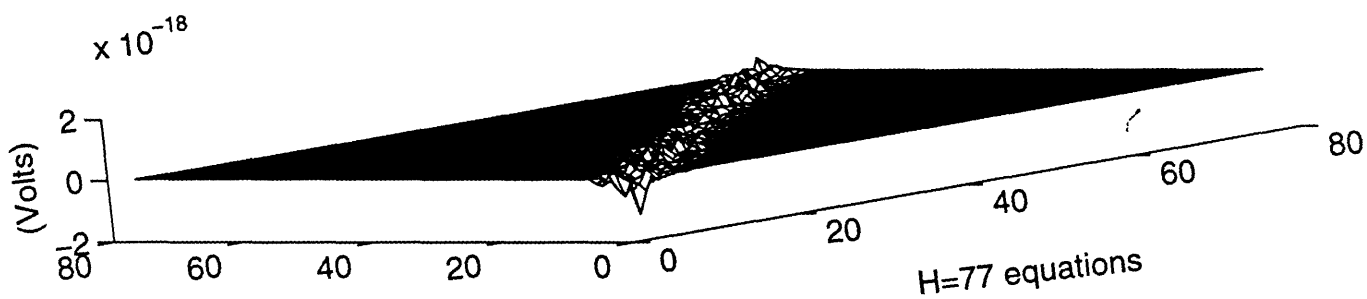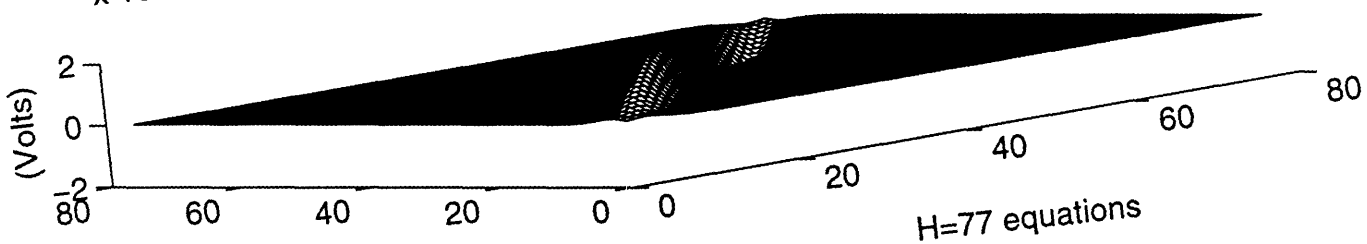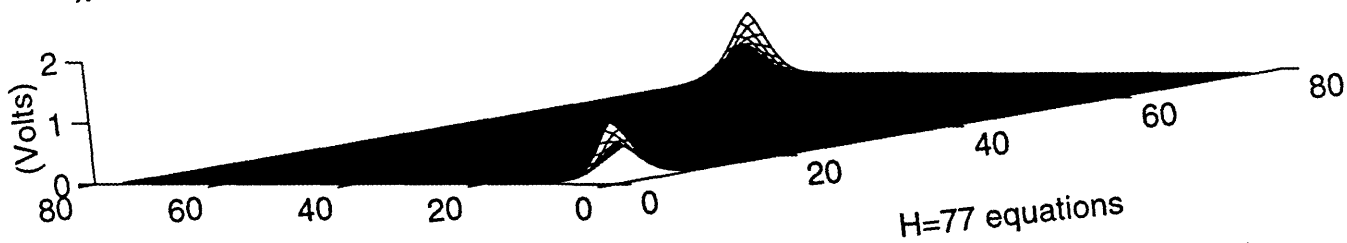
(f) H=77 output potentials

Figure 4.1, continued: Changes in output potential predicted by the linearized system $\mathbf{Ax=b}$, $(\mathbf{A} \equiv (\mathbf{e}_m .^* \mathbf{v}^d)^T$, $1 \leq m \leq H$ and $1 \leq d \leq H$, $\mathbf{x} \equiv \text{diag}(\delta\mathbf{G})$, and $\mathbf{b} \equiv -\delta v^d_{meas,m}$, $1 \leq m \leq H$ and $1 \leq d \leq H)$. The vector $\mathbf{x}$ is given in (a), (b), and (c), and the $\mathbf{b}$'s are given by (d), (e), and (f), respectively. The output potential vector, $\mathbf{b}$, has been made into a matrix so that one axis of (d), (e), and (f) corresponds to the output potentials due to a single source, and each single step of the other axis reveals output potentials due to each new source.

50

Even though we assemble many more equations than there are unknowns to provide more information about the problem, the fineness of the discretization may cause many of the equations to be nearly dependent. This was mentioned in Section 3.4, and is referred to as 'rank deficiency.' Having fewer independent equations than unknowns is a tractability problem which is reflected in the condition number. When a matrix is singular (at least one of its columns is not independent of the others), it is assigned a condition number near infinity. An orthogonal matrix has a condition number equal to one.

4.3 Sensitivity Analysis

The Jacobian which was introduced as a result of Equation 4.5 describes the sensitivity of the resistive sheet to small perturbations in conductance. In this study, we are interested in the variation in sensitivity due to an increased number of current injection sites, within a constant grid discretization. Sensitivity can be measured with the condition number.

We perform simulations which are designed to demonstrate an improvement in the conditioning, and hence the sensitivity, of the problem as more injection sites are added. The motivation for this increase in the number of injection sites is developed in Section 3.4. Similar experiments have also been conducted by Dr. Arridge. He examines the singular value decomposition of a Jacobian matrix (derived from a perturbation approach, as ours is) for different depths of tissue [24, Section 7]. In this research, we are concerned with a matrix A, which we define to be the Jacobian of $R(x)i$ with respect to the conductance to ground at each node, for the nominal conductance matrix, with no noise. The condition number can be found only for square matrices, so our computer simulations demonstrate an improvement in the condition number of $A^T A$ from 2.2×10^{13} to 2.0×10^{10} to 4.6×10^9 when the spacing between the injection currents is decreased from every three input nodes to every two nodes to every

node. Thus, we expect an improvement in condition number with a decrease in the current injection spacing, although it is likely to approach some value asymptotically [20].

5. Signal Processing and Numerical Algorithms

In Section 4.2 we suggest circumventing a difficult matrix inversion, in solving the nonlinear inverse problem of finding a stationary point of $\Phi(\mathbf{x})$, by implementing a linear, iterative method. In this approach, each new update to the solution is computed by solving a linear least squares problem. This linear problem is constructed as a result of a perturbed version of the nonlinear problem and an assembly of all the possible combinations of linear equations we can bring together, according to the number of injection and measurement sites in the model.

This can be loosely referred to as signal processing due to the relevant issue of spatial sampling. This chapter describes an additional signal processing issue -- that of regularization, which addresses the rank deficiency problem -- along with specific details about the numerical algorithm we use to solve the nonlinear inverse problem iteratively.

The following sections begin with a description of the current progress of comparable research in reconstruction methods, first in the work of Dr. Simon Arridge of University College London, and then in our own study. In Section 5.2, we discuss an approach which we implement using the Gauss-Newton method. In Section 5.1 we discuss popular regularization methods used by Dr. Arridge, and, in Section 5.3, the leverage that regularization gives to both researchers in improving the conditioning of our respective, similar, iterative methods. This form of intelligent signal processing is expected to help a great deal in terms of extracting useful information from experimental measurements.

Some other possible approaches to the reconstruction are also discussed. These include a solution derived through an explicit formulation for the inverse of the conductance matrix, in Section 5.4, and a possible implementation of the popular GMRES algorithm to speed up each iteration of the linearized inverse problem, in Section 5.2.2. The chapter ends with an explicit comparison between the tolerable amount of noise predicted by this

study, along with a required photon count predicted by Dr. Arridge for adequate reconstruction.

5.1 Related Research

One of the earlier motivations behind Dr. Arridge's work is to validate the use of the diffusion approximation as a model for light transport and noise in this problem by comparing its results with those of the Monte Carlo method [13, 26, 34, 37].[12] This discrete stochastic formulation produces a probabilistic spatial allocation of photons at every iteration within a discretized medium, based on their initial distribution which is incident upon the medium. The stochastic model is based on the scattering and absorption coefficients and a random but forward-biased scattering angle.

The actual discrete process is a random walk: at each point, it defines the next scattering or absorption event for each photon in the model; the direction of those photons which are scattered and stay in the game (as opposed to being absorbed and gone forever from the model) is projected onto their next evaluation of the renewal process [37, Section 3.1]. The diffusion approximation does not follow individual photon histories as this intricate stochastic model does [24]. Arridge's results which are based on the finite element method and the diffusion approximation are shown to agree with the analytical formulation of the photon distribution in the limit of high mesh resolution [26].

Although the Monte Carlo method offers an excellent model for the actual scattering and absorption events, it is computationally unfeasible to use it in real-time applications [24, Section 3.1]. In addition, it can be applied only to an integrated intensity measurement model, due to the fact that it is concerned with counting photons.

---

[12] Dr. Arridge used a finite element method for solving this problem, with additive noise which was also predicted according to the diffusion approximation [37, Section 5.1].

Arridge also introduces the application of a perturbation approach toward a solution for the inverse problem and for finding the Jacobian matrix [24]. To solve for the perturbation in absorption, Arridge suggests either direct methods such as the Moore-Penrose inverse or iterative methods, such as gradient descent, coupled with a stochastic model of the problem [10].[13] An example of this second case is his use of the Newton-Raphson approach with regularization to minimize a cost function based on the maximum likelihood estimate of the measured output. He also suggests using the Gauss-Seidel method; it may be more desirable since it does not require storage of the entire Jacobian matrix and therefore costs much less space in memory [13, Section 4.2].

Arridge also suggests that it is possible to get an idea of the resolution limit for reconstruction of perturbations by examining the singular value decomposition of the perturbation operator, the Jacobian matrix [24]. We conduct two similar experiments, one of which is discussed in Section 4.3, and the other at the end of Chapter 3. His experiment examines Jacobian matrices which are defined by tissue slabs of different depths. He finds that the conditioning of the problem improves for thinner depths of tissue [24]. He further suggests that a coarser grid discretization may improve the conditioning of the inner product of the Jacobian with itself, since the Jacobian matrix is typically underdetermined [13, 25]. This sacrifices the accuracy which would be achieved with a finer grid, however, as we have already mentioned [26].

In future work, Arridge sees a high potential for reconstructions which rely on nonlinear methods [25]. He believes that measuring photon flux instead of photon density may improve the convergence of iterative methods from linear to quadratic speeds [26]. He also suggests that a higher-order model, such as one which seeks to determine the anisotropicity of scattering or the refractive index, could be implemented with the use of higher-order data [10, 25]. In addition, he expects that a more extensive use of a priori information should be helpful [13].

---

[13] For a formal definition please see Golub and Van Loan, p. 243.

Arridge further suggests that measurement methods which are not time-dependent will not be able to distinguish between changes in absorption and scattering [13]. This issue will become increasingly relevant as we understand more about their dynamics within tissue. Right now, the distinct contributions of each are difficult to differentiate [30].

As an example of a time-dependent measurement method, n^{th}-order moments of the time of flight of photons could be calculated. They would produce numerical results over a smaller dynamic range than would be required by the integrated intensity measurement model [32]. A couple of Dr. Arridge's articles show both theoretically and experimentally that a greater penetration depth can be achieved when trying to detect absorption in a scattering medium by using the mean time of flight rather than integrated intensity as a measurement model [30, 31, 32]. He also derives a precise theoretical relationship between mean time of flight of photons (which is relevant to the optical pathlength of the medium) and the phase shift measured at the tissue output from a frequency modulated input signal [32].

Another possible approach to the inverse problem is referred to as the 'double constraint' method in Electrical Impedance Tomography. It involves the use of output measurements as boundary conditions and solves for the interior optical parameters of the medium. Arridge doesn't think that it has been done yet for this type of problem [13].

Arridge's work is extensive in this field, but this research problem is much richer in its complexity which has *yet* to be well-understood. The understanding and refining of the best reconstruction algorithms and CPU speed should proceed steadily, accompanied by increased knowledge about the related optical parameters and their relative contributions. Soon this detection method should reach a better operational level with the necessarily strong knowledge base and computational means. The labor between here and there is in searching for signal processing solutions which will enable medical professionals to use this technology to distinguish necessary information from

the only affordable measurements (which contain little apparent data), and in the precision of detection methods which directly affect the level of accuracy in measurements.

5.2 The Gauss-Newton Iterative Method

But how did we get here already? We have stated that we approach the solution to this nonlinear least squares problem using an iterative method. The iterative solution will update our guess at a nearby stationary point of the nonlinear least squares cost function, where the new guess is referred to as $\mathbf{x}^{k+1}$. We could choose a *gradient-based* method, for example, in order to solve the linear least squares problem at each iteration. This general class of algorithms for iterative descent represents an important conceptual idea in unconstrained minimization [5, Section 1.2]. The simplest of these is the steepest descent method [5, Section 1.2].[14] Given a scalar cost function at the kth iteration, $\Phi(\mathbf{x}^k)$, the steepest descent iterate is updated according to:

$$\mathbf{x}^{k+1} = \mathbf{x}^k - \alpha^k (\nabla\Phi(\mathbf{x}^k)), \qquad (5.1)$$

where α^k is a scaling stepsize. In addition, we can simplify Equation 3.7 so that it is now:

$$\Phi(\mathbf{x}^k) = \|\mathbf{f}(\mathbf{x}^k) - \mathbf{y}\|^2,$$

where $\mathbf{f}(\mathbf{x}^k)$ is equal to $R(\mathbf{x}^k)\mathbf{i}$, for all of the possible $\mathbf{i}$'s, and $\mathbf{y}$ is the measured value of output potential at every output node due to injection at every input node. Equation 5.1 is easy to solve since we know that the gradient of the cost function at $\mathbf{x}^k$ is equal to:

$$\nabla\Phi(\mathbf{x}^k) = 2[\mathbf{J}(\mathbf{f}(\mathbf{x}^k))]^{\mathrm{T}}(\mathbf{f}(\mathbf{x}^k) - \mathbf{y}). \qquad (5.2)$$

But this method is problematic since the Jacobian of $f(x^k)$, which we defined in Section 4.1, is poorly conditioned.[15] Poor conditioning implies that elliptic level curves, which represent sets of values for x^k for which $\Phi(x^k)$ is constant, will be very elongated. Then the steepest descent search direction is nearly orthogonal to the direction which leads to the minimum [5, Section 1.2]. The search path could follow far along the direction of steepest local gradients before approaching the local stationary point of the nonlinear cost function. This is referred to as zigzagging, and takes place when local gradients are steeper than the path toward the stationary point, so that the iteration zigzags along locally as it makes its way to the stationary point. The result is very slow convergence.[16] In a well-conditioned problem, the descent search directions are more direct, and the elliptical level curves are more circular.

An alternative to steepest descent, which is more complex but less problematic, is Newton's method. Its goal is to set the gradient of the cost function equal to zero. To do so, consider the first-order Taylor expansion of the gradient of the cost function about an estimate, x^k:

$$\nabla\Phi(x^k + \Delta x^k) \approx \nabla\Phi(x^k) + [J(\nabla\Phi(x^k))](\Delta x^k), \qquad (5.3)$$

where $\Delta x^k \equiv x^{k+1} - x^k$. Newton's method is realized by setting Equation 5.3 equal to zero to get:

$$-\nabla\Phi(x^k) = [J(\nabla\Phi(x^k))](\Delta x^k), \qquad (5.4)$$

where the gradient at x^k, $\nabla\Phi(x^k)$, is given by Equation 5.2. Rearranging terms and using the definition of Δx^k gives:

---

[14] We define the ith entry of the gradient of a scalar function, $g(x)$: $\Re^N \to \Re$, as:
$$[\nabla g(x)]_i = \frac{\delta g(x)}{\delta x_i} .$$

[15] Recall the definition of conditioning from the end of Section 3.4.
[16] We should mention that we are not guaranteed to be following the path to a global minimum here. The gradient-based solutions we discuss may converge to a local minimum, maximum, or saddle point.

$$\mathbf{x}^{k+1} = \mathbf{x}^k - (\mathbf{H}(\Phi(\mathbf{x}^k)))^{-1}(\nabla\Phi(\mathbf{x}^k)).^{[17]} \qquad (5.5)$$

This approach gets more directly to the point of what we are looking to find, a location $\mathbf{x}$ at which the cost function, $\Phi(\mathbf{x})$, is stationary. The convergence of Newton's method is generally asymptotically fast, since the steepest descent path is avoided in pursuit of the actual minimum to which it would have eventually taken you [5, Section 1.2]. Newton's method is desirable because of this knack for avoiding the zigzagging problem [5, Section 1.2]. The method of conjugate gradients also avoids this and was investigated in Dr. Arridge's research, but he found it to have slow convergence, as did, obviously, the method of steepest descent [13, 38].

Unfortunately, Newton's method requires the calculation of the Hessian of $\Phi(\mathbf{x}^k)$, which is computationally difficult. A simplification which imitates the performance of Newton's method would be helpful at this juncture and the Gauss-Newton method is just that [5, Section 1.2]. Gauss-Newton relies on the assumption that:

$$\Phi(\mathbf{x}^k + \Delta\mathbf{x}^k) \approx \left\| \mathbf{f}(\mathbf{x}^k) + \left[\mathbf{J}(\mathbf{f}(\mathbf{x}^k)) \right]\Delta\mathbf{x}^k - \mathbf{y} \right\|^2,$$

so that the minimization of $\Phi(\mathbf{x}^k + \Delta\mathbf{x}^k)$ will find the closest approach to equality in the following equation:

$$\left[\mathbf{J}(\mathbf{f}(\mathbf{x}^k)) \right]\Delta\mathbf{x}^k = \mathbf{y} - \mathbf{f}(\mathbf{x}^k). \qquad (5.6)$$

With this step, we have an expression which is linear in $\Delta\mathbf{x}^k$ [20]. If we refer to the Jacobian in the brackets in Equation 5.6 as simply '$\mathbf{J}_k$,' then the Gauss-Newton method is:

---

[17] We define the [i,j] entry of the Hessian matrix of the scalar function, $g(\mathbf{x}^k)$, as:
$$\left[\mathbf{H}(g(\mathbf{x}^k)) \right]_{i,j} = \frac{\delta^2 g(\mathbf{x}^k)}{\delta x_i^k \delta x_j^k}, \ 1 \le i,j \le N \text{ and } \mathbf{H}(g) \in \mathfrak{R}^{N \times N}.$$

$$\mathbf{x}^{k+1} = \mathbf{x}^k - \alpha^k \left(\mathbf{J_k}^\mathsf{T} \mathbf{J_k} \right)^{-1} \mathbf{J_k}^\mathsf{T} \left(\mathbf{y} - \mathbf{f}(\mathbf{x}^k) \right).$$

It is similar to Newton's method except that it does not require the calculation of a Hessian.

The Gauss-Newton method will find a local stationary point for any arbitrary cost function, even in poor conditions such as when the perturbation is large or the cost function is not smoothly varying. In this problem, it should be taking advantage of the fact that we expect the solution $\mathbf{x}$ to be a small perturbation, and that the cost function may be locally smooth so that the linearity assumption is a good one. In section 5.3 we explain the use of a scale factor, α^k, for when these two characteristics are absent.

Under the right circumstances, Newton's method is possibly the fastest of the gradient descent methods, although it is also the most complicated; and steepest descent is typically the slowest [5, Section 1.2]. The 'circumstances being right' typically means that the initial guess is chosen to be within a neighborhood of the local minimum, so that there is superlinear convergence. In the case where the iteration begins within a neighborhood of the solution, Newton's method should take only a handful of iterations to converge; otherwise, convergence is superlinear once the solution gets within this neighborhood [5, p. 83]. We may be steered toward an undesired stationary point by a Newton-like method. But the hope is that our initial guess, the nominal conductance, quickly brings us into the neighborhood of the minimum we seek.

5.2.1 Gauss-Newton Simulation Results

Our reconstruction algorithm uses a Gauss-Newton iterative method for the least squares problem, with Marquardt regularization, which is introduced in Section 5.3. The resistor values in our circuit model correspond to optical parameters for healthy breast tissue, and simulate a perturbation in the vertical

60

and horizontal conductances due to a stronger absorbing material where a tumor is located [46, Section IV, 42]. This should reflect the high absorption of a material we can use to tag tumors and make them more apparent. Using an anisotropy constant within the known range for breast tissue, we can calculate the corresponding scattering coefficient as well.[18] The optical parameters are given in Table 5.1, below, where the '≈' indicates that we have calculated the

Transport Cross Section	Absorption Coefficient	Scattering Coefficient
0.2578 mm^{-1}	0.0668 mm^{-1}	≈3.82 mm^{-1}

Table 5.1: Optical parameters for healthy breast tissue

approximate scattering coefficient ourselves. The actual horizontal and vertical conductance values for individual resistors, nominal and perturbed, are given in Table 5.2. When the absorption coefficient is perturbed at grid node k, the

	Horizontal Conductance (mho)	Vertical Conductance (mho)
Nominal	0.97	0.8
Perturbed	0.82	1.4

Table 5.2: Horizontal and Vertical Conductances

corresponding diagonal of the conductance matrix becomes:

(# adjoining horizontal neighbors)*(horizontal conductance) + vertical conductance.

Nodes of the conductance matrix which represent the connection between node k and a horizontal neighbor, according to their coordinates within the matrix (as defined in Chapter 1) take on the value:

---

[18] The transport cross section is given by $\mu_{tr} = \mu_s(1-g) + \mu_a$, where g is the anisotropy constant [45, p. 1328].

-(horizontal conductance)

in the appropriate entry of the matrix. Using a perturbation approach for the construction of the Jacobian, we attempt to use it to reconstruct a perturbation in *only* the vertical conductances. This is not precisely correct since the horizontal conductances actually change, too, according to Chapter 2. However, adding terms in the Jacobian to account for the derivative with respect to the horizontal conductances makes the problem much larger, computationally.

The reconstruction is sensitive to the absorption coefficient's not being too large; when the perturbation in absorption is too large, the algorithm mistakenly detects two peaks when there is really just one. We think it's possible that if the perturbation is much too large, it detracts from the amount of exiting output potential, making the problem more difficult.

When the absorption coefficient is equal to 0.1 mm^{-1} (about twice its nominal value), two distinct nodes of absorption can be resolved when located near the center of the grid. Assuming that the limiting noise in the experimental model is due to quantization, we vary the additive white Gaussian noise (independent values are added at each simulated output measurement) according to the simulated number of bits of quantization [35]. There is also noise due to pixel mismatch, which is difficult to model but important to account for by calibrating the devices beforehand. The variance of the noise in a (B+1)-bit quantizer can be computed according to:

$$\sigma^2 = \frac{2^{-2B} X_m^2}{12}.$$

X_m is the full-scale potential of what is being quantized, and in our case this is the nominal potential at a particular output node due to injection of current at the input node in question [49]. The lowest number of bits of quantization noise which can be resolved by the reconstruction algorithm is about *fifteen*, assuming that all emitted electrons are collected at the output. The diagonal of the

conductance matrix is made into a matrix of the same size as the grid so that the plot easily readable. The indexing is as in Figure 3.1. The actual diagonal of a perturbed conductance matrix is shown in Figure 5.1. The perturbation is due to a change in the absorption coefficient. Sample reconstructions for quantization noise due to fourteen-, fifteen-, and sixteen-bit A/D converters are shown in Figures 5.2, 5.3, and 5.4, respectively.

We also conducted simulations in which only the vertical conductances were perturbed, and, as in the previous simulation, only the vertical conductances are reconstructed. When compared to the previous example, this proves to be a more *difficult* problem with the *same* perturbation in absorption, since the perturbation in this case is accurately resolved with the quantization noise corresponding to a *seventeen*-bit A/D converter. The actual vertical conductance is perturbed in the same location as in Figure 5.1, but it is now more apparent. The diagonal of the conductance matrix is shown in Figure 5.5, with the same indexing as in Figure 3.1. Results, the constructions for sixteen, seventeen, and eighteen bits of quantization noise, are shown in Figures 5.6, 5.7, and 5.8, respectively.

Why is the perturbation in vertical conductance so much more difficult to reconstruct when it is realized by perturbations in only the vertical conductance? It certainly appears to be a less difficult problem, *visually*, when one compares Figures 5.1 and 5.5. It is possible that our less accurate description of the actual physical process which takes place (a perturbation of both the horizontal and vertical conductances) makes it more difficult to resolve the conductances along the diagonal.

5.2.2 Gauss-Newton and the GMRES Algorithm

The Gauss-Newton algorithm, although a simplification from the nonlinear least squares version of the problem, still faces the task of solving many equations in many unknowns. One way to get around this computational
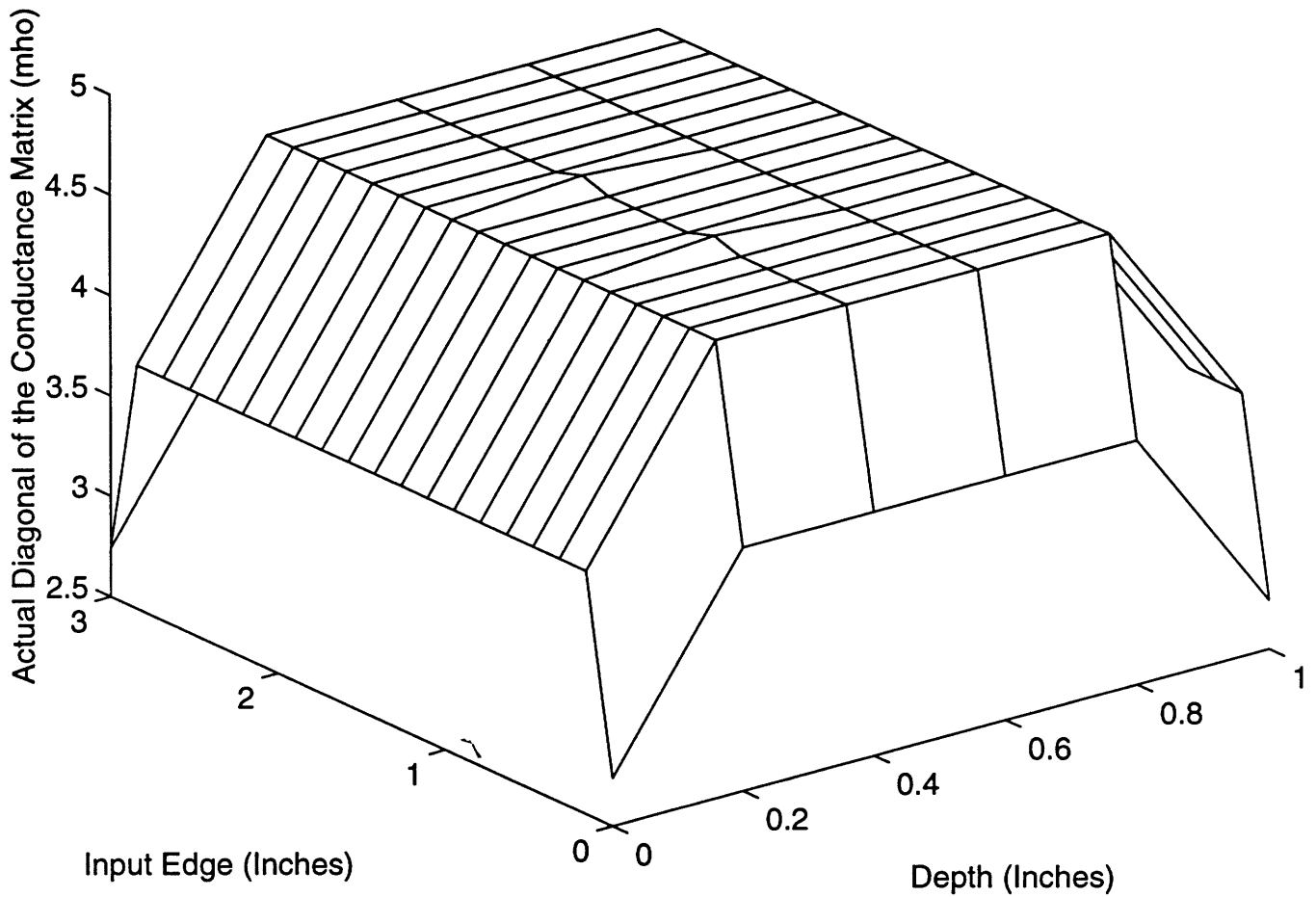
Figure 5.1: At most nodes, actual conductance along the diagonal of the conductance matrix due to nominal absorption = 3.96 mho (it varies at the grid boundaries), perturbed absorption = 5.36 mho; perturbed absorption coefficient = .1195 mm^{-1}, perturbed transport cross section = .3039 mm^{-1}. Only the vertical conductances are perturbed. Values are given according to Table 5.2 and the formulae beneath it.
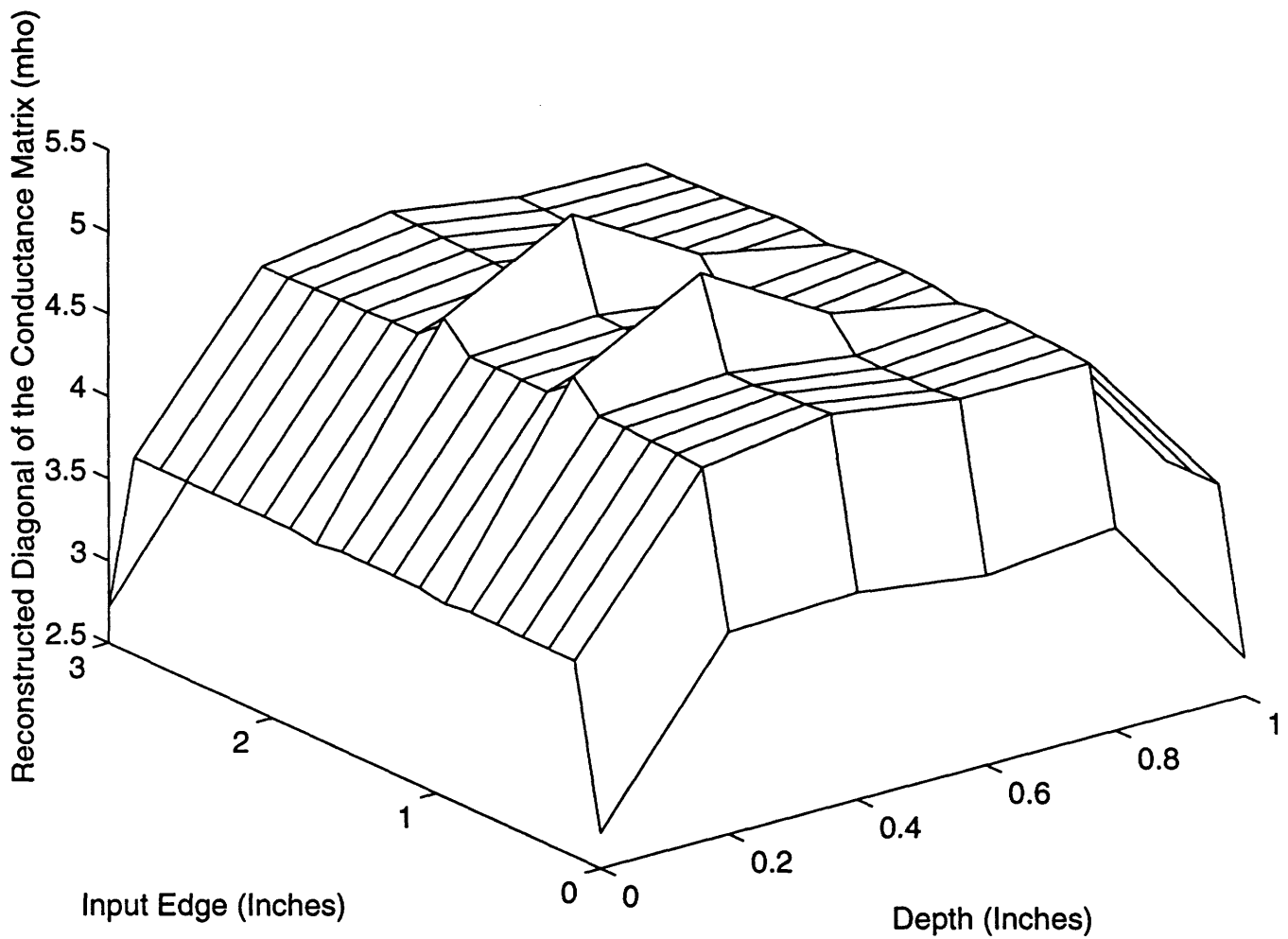
Figure 5.2: Reconstructed conductance along the diagonal of the conductance matrix due to 14-bit A/D converter quantization noise and actual conductances given in Figure 5.1.
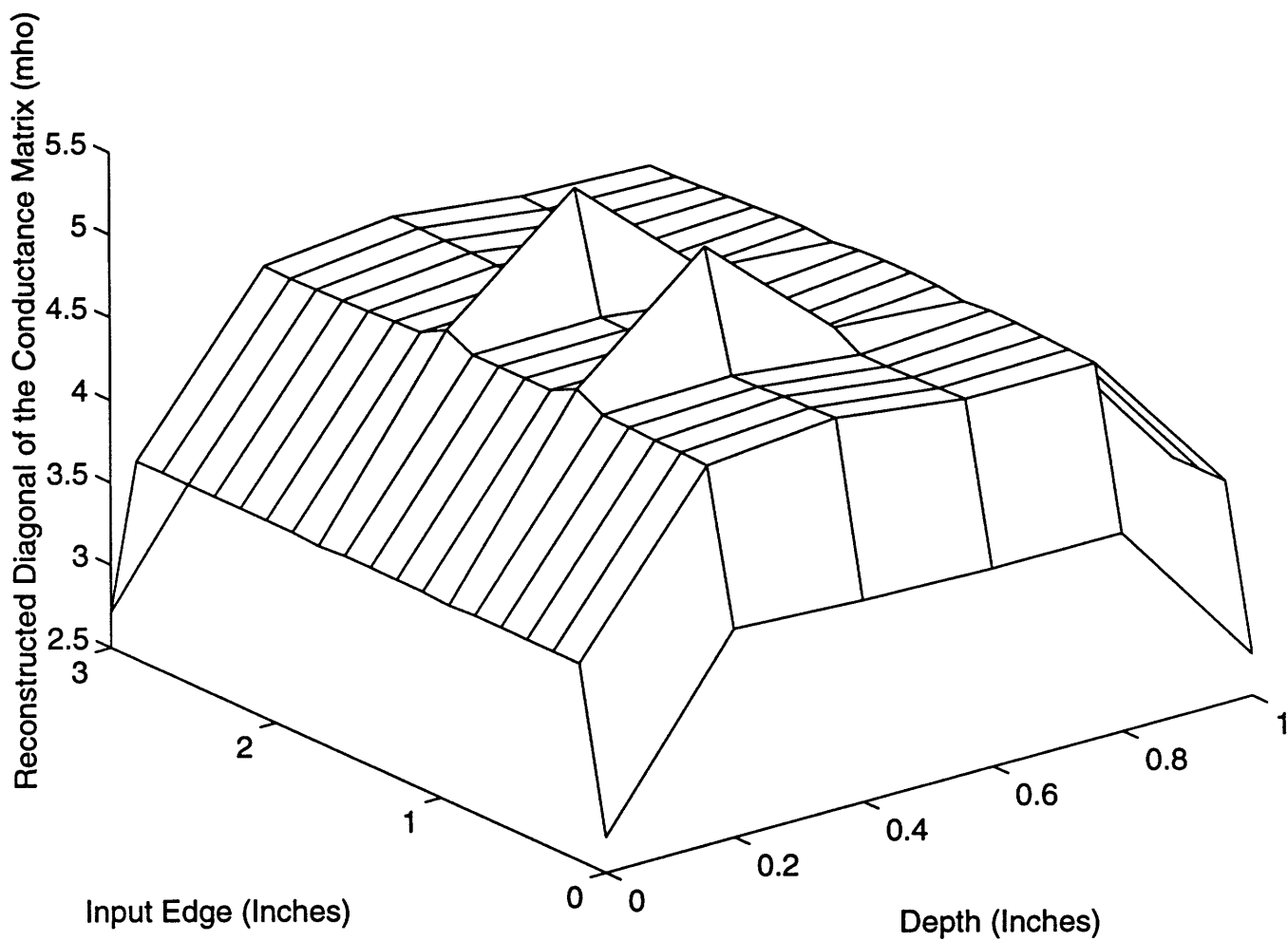
Figure 5.3: Reconstructed conductance along the diagonal of the conductance matrix due to 15-bit A/D converter quantization noise and actual conductances given in Figure 5.1.
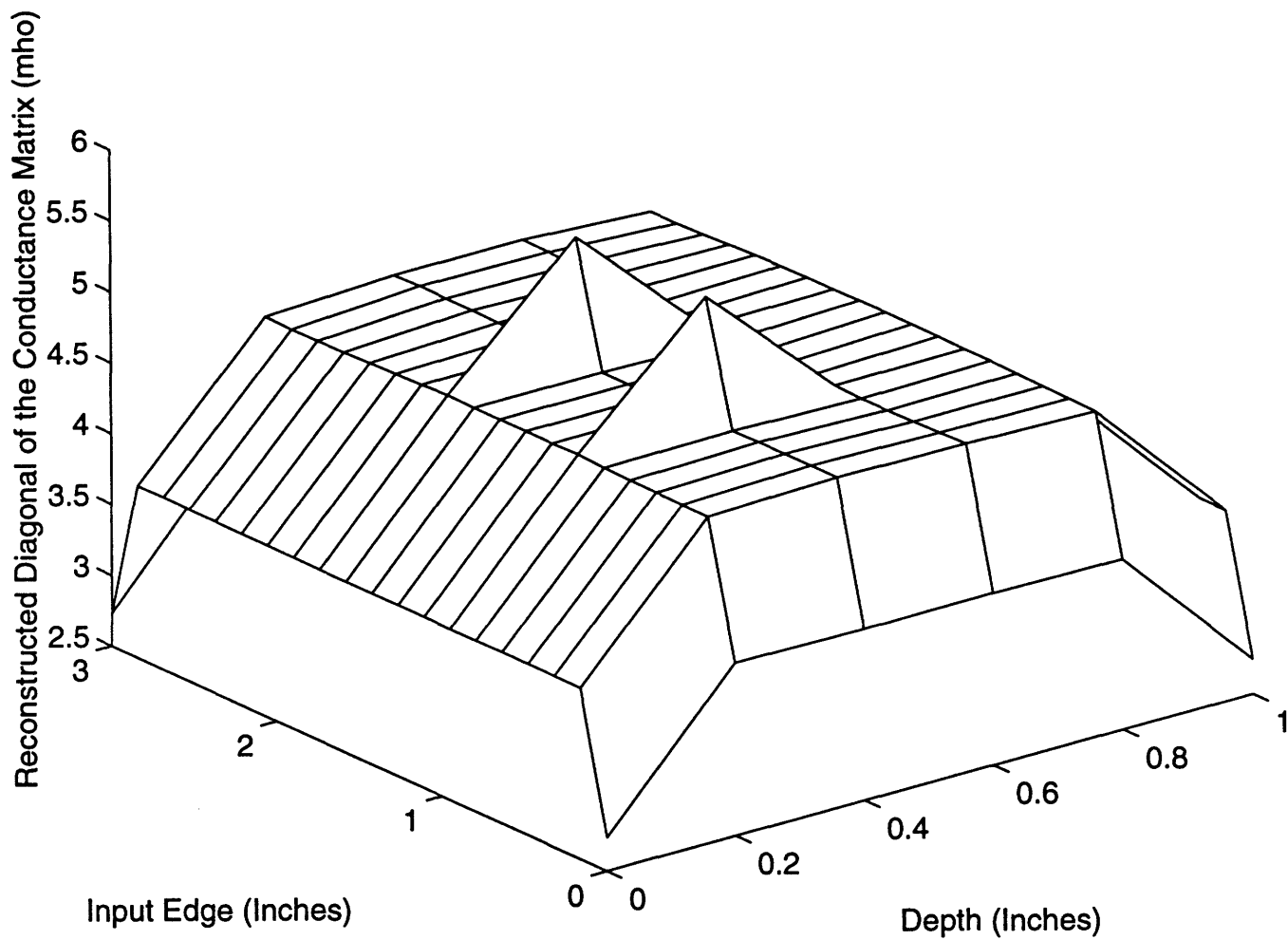
Figure 5.4: Reconstructed conductance along the diagonal of the conductance matrix due to 16-bit A/D converter quantization noise and actual conductances given in Figure 5.1.
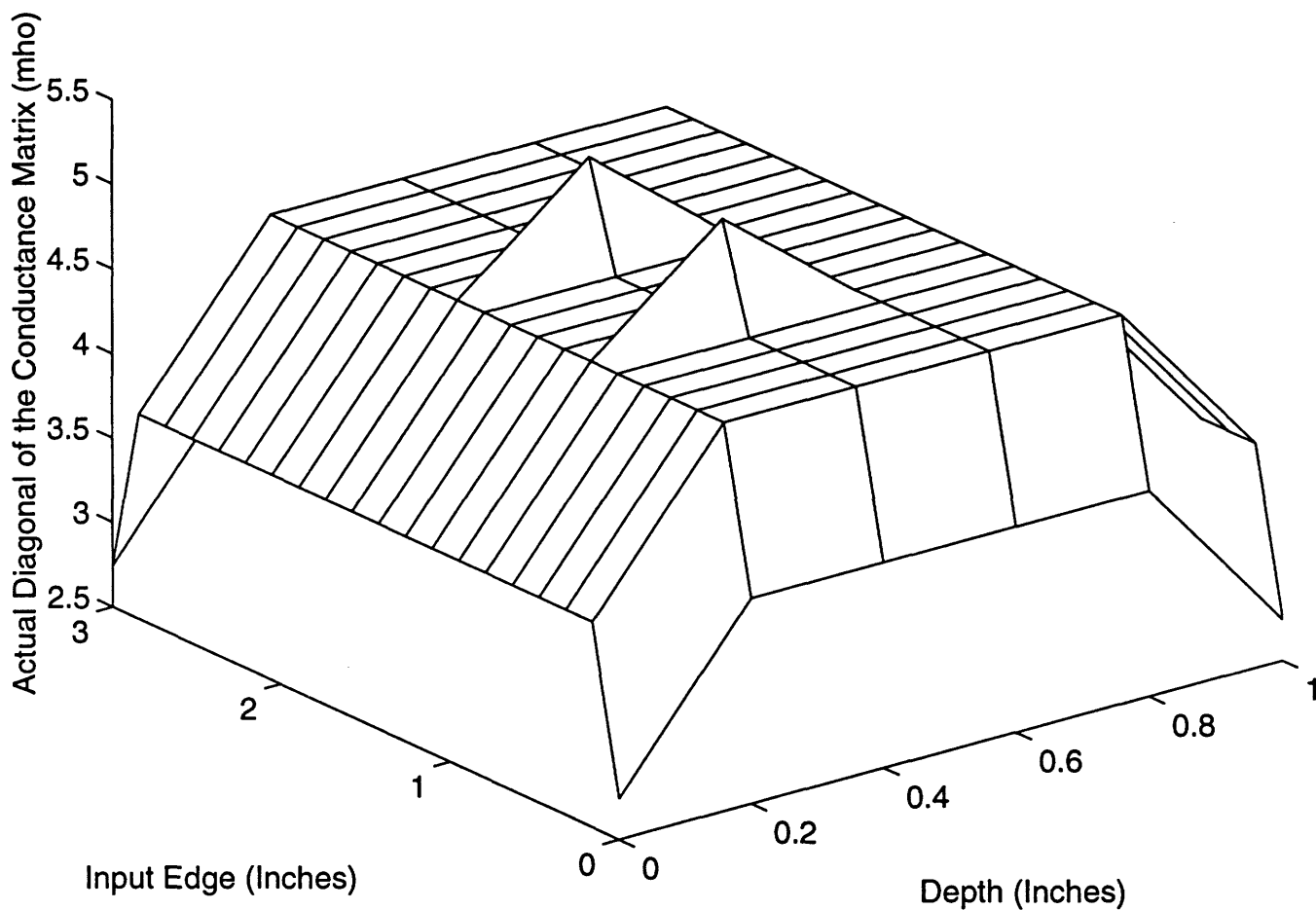
Figure 5.5: At most nodes, actual conductance along the diagonal of the conductance matrix due to nominal absorption = 3.96 mho (it varies at the grid boundaries), perturbed absorption = 4.68 mho; perturbed absorption coefficient = .1195 mm^{-1}, perturbed transport cross section = .3039 mm^{-1}. Vertical and horizontal conductances are perturbed so that horizontal conductances neighboring a perturbed node change from 0.97 mho to 0.8 mho (not shown). Values are given according to Table 5.2 and the formulae beneath it.
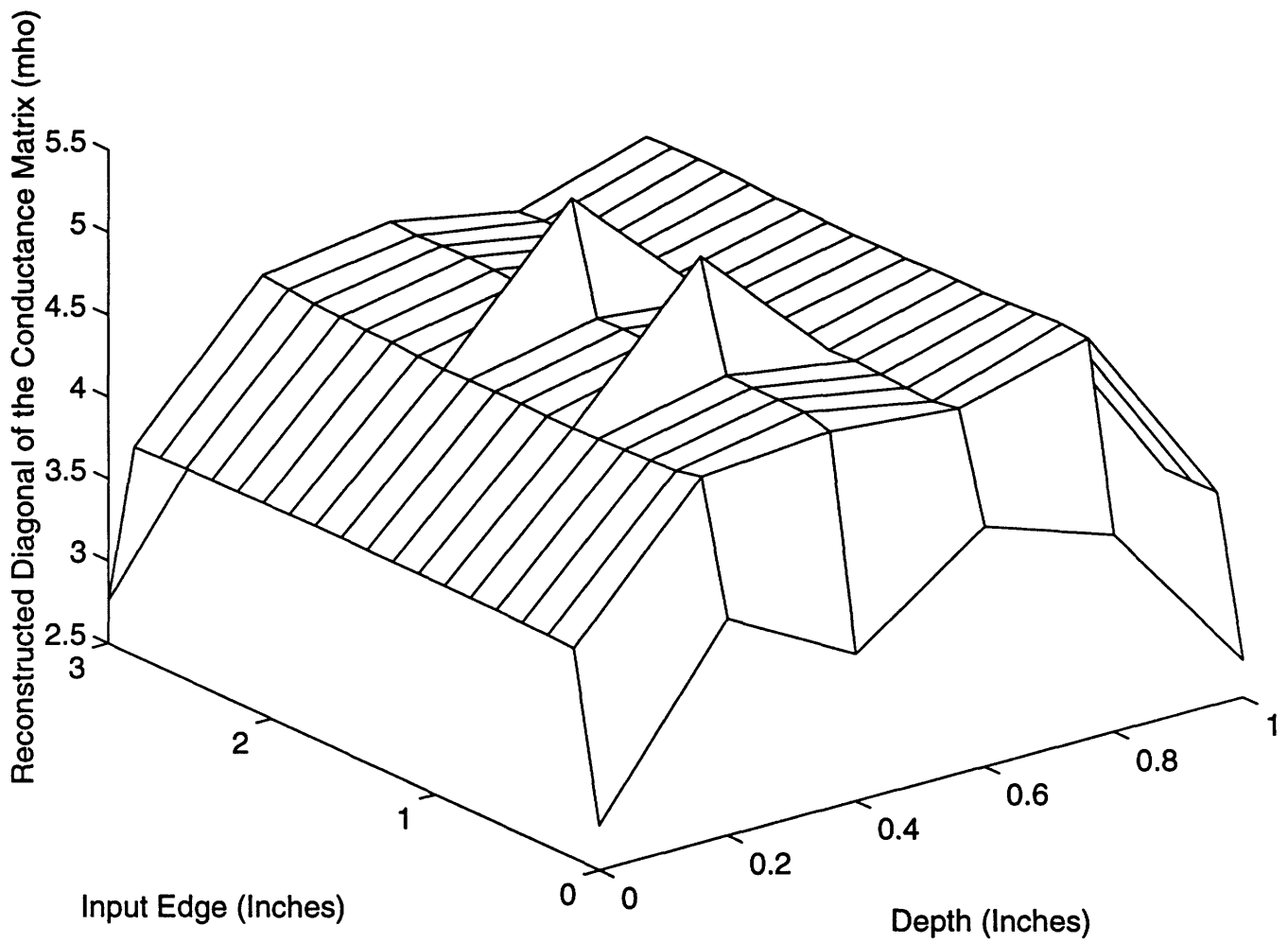
Figure 5.6: Reconstructed conductance along the diagonal of the conductance matrix due to 16-bit A/D converter quantization noise and actual conductances given in Figure 5.5.
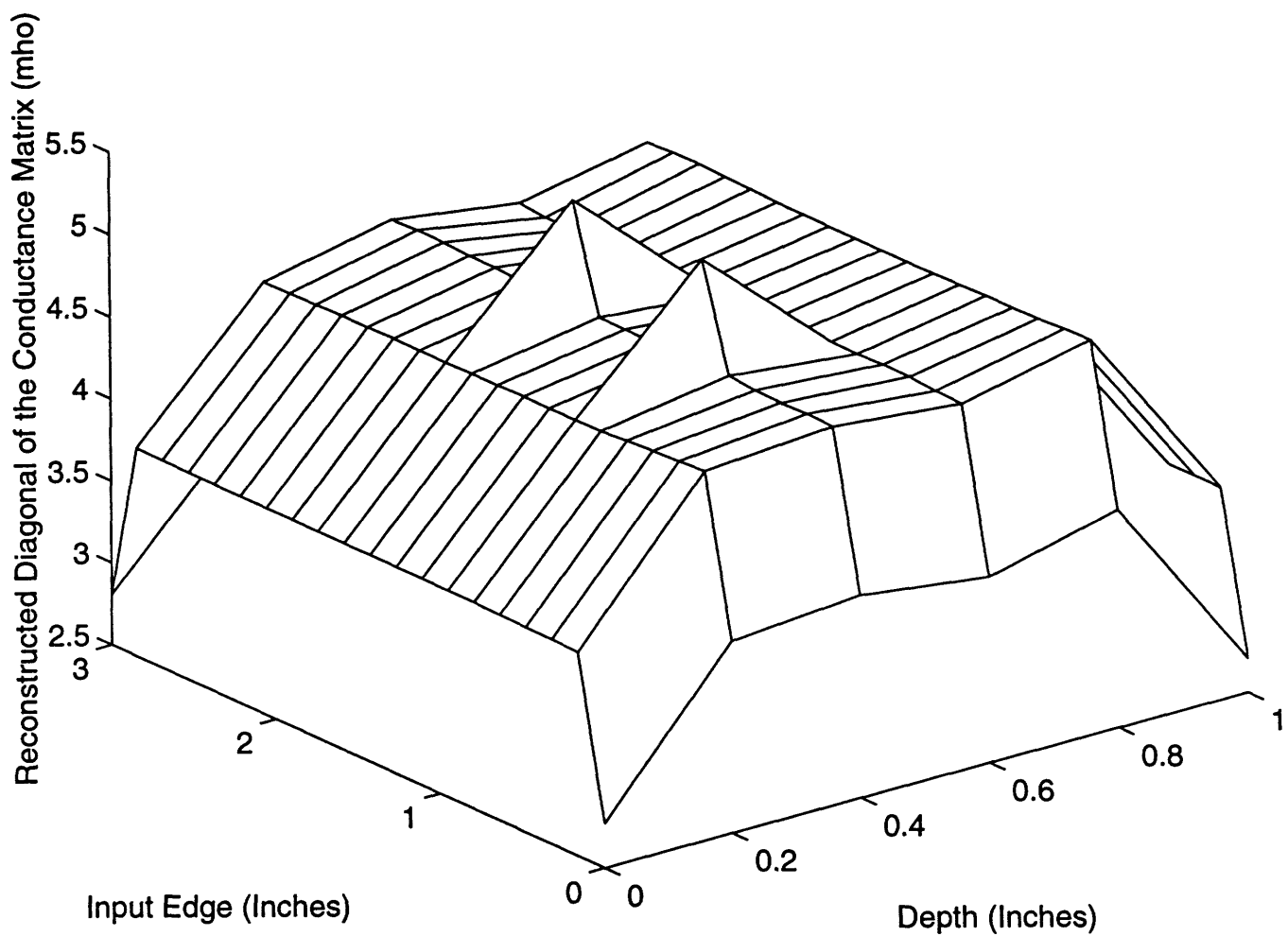
Figure 5.7: Reconstructed conductance along the diagonal of the conductance matrix due to 17-bit A/D converter quantization noise and actual conductances given in Figure 5.5.
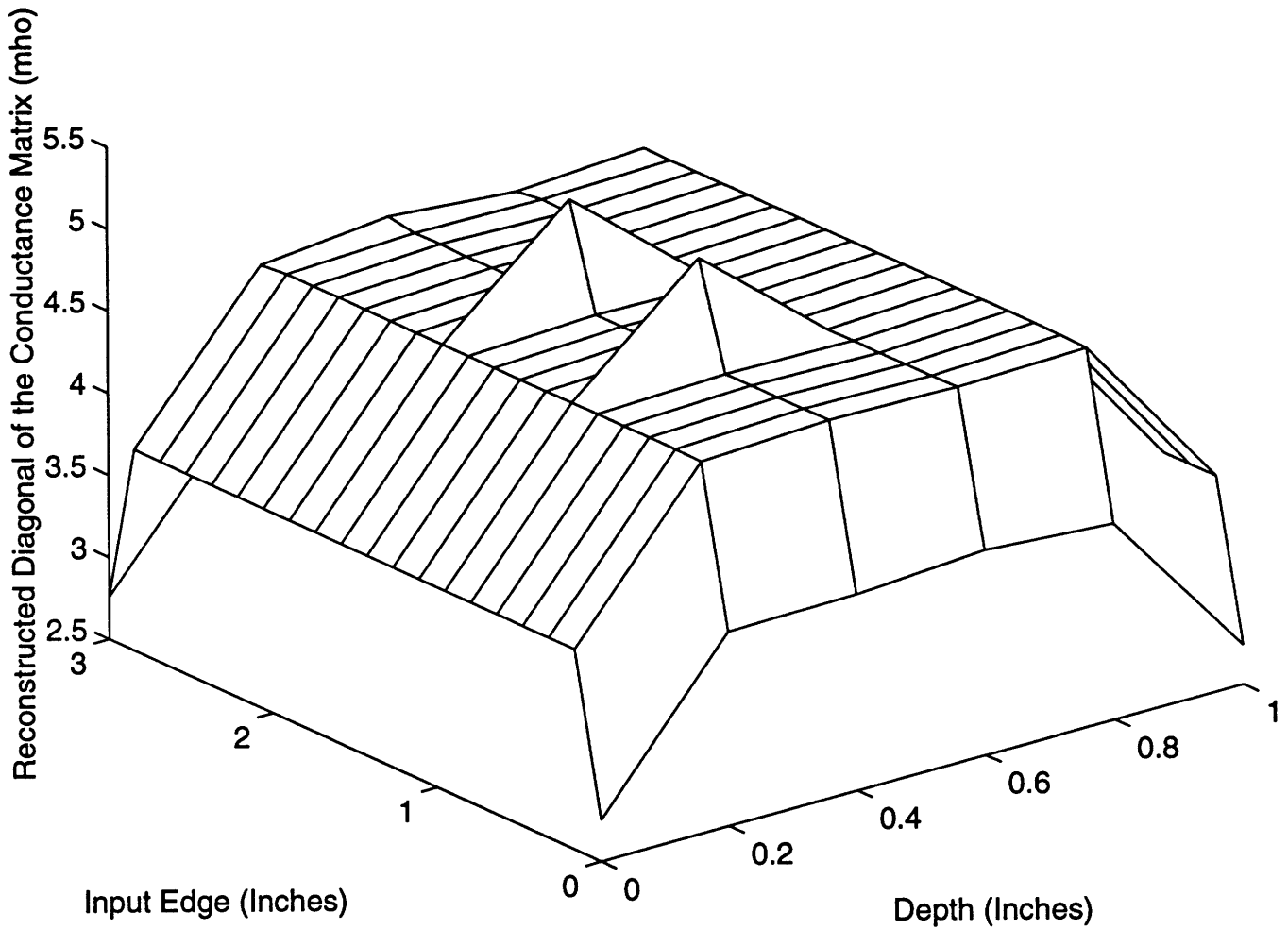
Figure 5.8: Reconstructed conductance along the diagonal of the conductance matrix due to 18-bit A/D converter quantization noise and actual conductances given in Figure 5.5.

computational bottleneck is to use the GMRES algorithm to solve the system of linear equations. GMRES has the advantage of being able to solve a linear system $Ax = b$ for a nonsingular, nonsymmetric, nxn matrix, A, in at most n iterations [6, Section 3.1], so that the slightly less than n^2 operations required by MATLAB to solve n equations in n unknowns can be replaced with many less than n^2 operations. This makes each Gauss-Newton step that much faster, speeding up every iteration toward the nonlinear solution.

The GMRES algorithm solves a linear least squares problem over a series of basis vectors. The first basis vector is the first residual error vector. This is the residual of Equation 5.6. Each successive basis vector is determined by multiplying the A matrix onto the previous basis vector, orthogonalizing with respect to the previous basis vectors, and normalizing the resultant vector. We were able to implement GMRES in the later portion of our research. We found that the more influential computational bottleneck is due to the formation of the Jacobian matrix, and further performance improvements are recommended in Chapter 6.

5.3 Establishing the Fundamental Limits of Resolution Using Regularization

The nonlinear inverse problem is highly sensitive, and this sensitivity carries into the linear least squares problem as well. The Gauss-Newton method does not give a solution set unless it is modified so that the inner product of the Jacobian matrix with itself is nonsingular. We first attempted to make this inner product nonsingular by taking the singular value decomposition of the inner product, removing the singular values which were very close to zero, and inserting the remaining singular values back into the triple product to reconstruct the inner product. This procedure accomplishes the goal of nonsingularity and hence makes the iterations possible, but valuable high frequency information is lost when the very small singular values (and hence

their corresponding singular vectors when reassembling the triple product) are removed. This difficulty brings us to look at regularization as a signal processing improvement to the problem, since it offers help in making a poorly-posed problem into a well-posed one, as reflected in the condition number of the discretized problem [27, p. 8].

In this instance, regularization makes the problem more well-posed by decreasing the number of possible solutions. Whereas before regularization we were concerned with the minimization of $\Phi(\mathbf{x}^k)$, we are now concerned with the minimization of the quantity:

$$g(\Delta\mathbf{x}^k) = \left\|\mathbf{f}(\mathbf{x}^k) + \mathbf{J}_k\Delta\mathbf{x}^k - \mathbf{y}\right\|^2 + \varepsilon\left\|\Delta\mathbf{x}^k\right\|^2 \qquad (5.7)$$

over $\Delta\mathbf{x}^k$. Differentiating Equation 5.7 with respect to $\Delta\mathbf{x}^k$, setting the result equal to zero, and solving for $\Delta\mathbf{x}^k$, the minimization of $g(\Delta\mathbf{x}^k)$ will result in:

$$\Delta\mathbf{x}^k = (\mathbf{J}_k^{\mathsf{T}}\mathbf{J}_k + \varepsilon\mathbf{I})^{-1}\mathbf{J}_k^{\mathsf{T}}(\mathbf{y} - \mathbf{f}(\mathbf{x}^k)). \qquad (5.8)$$

We'll refer to the quantity which is inverted as $\mathbf{C}_k$:

$$\mathbf{C}_k = \mathbf{J}_k^{\mathsf{T}}\mathbf{J}_k + \varepsilon\mathbf{I}.$$

Now the problem is more well-posed, since we narrow down the search for possible solution vectors by using a weighted tradeoff in preference between those solutions which are small in length and those which minimize $\Phi(\mathbf{x}^k)$. The regularization constant, ε, controls the relative influence of these two components in the revised cost function, $g(\Delta\mathbf{x}^k)$.

The secondary effect of regularization is to improve the conditioning of $\mathbf{J}_k^{\mathsf{T}}\mathbf{J}_k$ for better performance of numerical methods in solving the linear least squares problem (we use regularization only in the linear least squares problem). We explain below just how this happens.

Since regularization is used in reconstruction methods, it is sensible to compare the resolution of different models of grid spacings and injection current patterns after they have been regularized. That is, we would like to examine the

73

condition number of C_k when solving $g(\Delta x^k)$, where the regularization constant is effectively being added in all along the diagonal of $J_k^T J_k$.

The matrix C_k is symmetric positive definite since the inner product $J_k^T J_k$ is symmetric positive semidefinite and εI is nonzero. This means that the singular values of C_k are the eigenvalues of C_k, which is the same as [εI plus the eigenvalues of $J_k^T J_k$]. The condition number, the ratio of largest to smallest singular values, of $J_k^T J_k$ is $\frac{1}{10^{-16}}$ (where 1 is the largest singular value of C_k and 10^{-16} is the smallest), or 10^{16}. With regularization the condition number becomes $\frac{\varepsilon+1}{\varepsilon+10^{-16}}$, and if ε is much larger than 10^{-16}, the condition number has improved and is now approximately equal to $1/\varepsilon$!

We have mentioned that the regularization constant can be chosen according to a statistical model of the problem. In this instance, the regularization constant acts as a prior condition on the variance of the solution. By comparing the solution Δx^k due to minimizing the cost function $g(\Delta x^k)$ with the Δx^k we would get by minimizing a stochastic model of the problem which has knowledge of the noise variance, we can relate the regularization constant to a prior condition on Δx^k.

We can estimate the variance of the noise due to a single input source based on existing data. The model can then be expanded to account for noise variance due to our *multiple* sources and we can let this variance contribute to the choice of regularization constant in the Miller criterion, the ratio of the norm of the standard deviation of the data to that of the current estimate of the solution [13, Section 4.3].

Alternatively, the regularization constant can be chosen according to the Marquardt method. We used this method and added a scaling within the Marquardt algorithm, so that Δx^k's (solutions to the linear least squares problem which we solve at each iteration of the nonlinear least squares problem) which

74

are good but too large to reduce $g(\Delta x^k)$ aren't simply thrown away. We make ten attempts at scaling the Δx^k down by a factor of 0.5 (this is actually the α^k of the Gauss-Newton algorithm). If none of these scale factors (α^k being equal to $(0.5)^n$, for n=1 to 10), is successful at producing a Δx^k which will decrease the residual, the first 'Else' in number 2 in the algorithm below ends, with n = 11, and we compute another Δx^k from a larger regularization constant. For the kth linear least squares solution, we choose the regularization constant (i.e., ε in Equation 5.8) according to the following modified Marquardt algorithm:

1. $\varepsilon^1 = 0.01$; $\Delta x^0 = 0$; k=1; The first (k = 1) residual in Equation 5.6 is therefore the difference between the measured output potential and the output potential due to the nominal conductance matrix;

2. While the reconstructed solution does not look satisfactory:

    Use Equation 5.8 to solve for Δx^k

    Compute the residual in Equation 5.6

    If it's less than the previous residual then k = k + 1 and $\varepsilon^k = \varepsilon^{k-1}/10$

    Else

        n = 1

        While n<11 and the current residual is bigger than the previous one,

            $\Delta x^k = (0.5)^* \Delta x^k$

            Compute the new residual in Equation 5.6 with this new Δx^k

        End

    End

    If n == 11 then the scaling by α^k wasn't successful in reducing the residual from the last iterate, so recompute Δx^k with a larger ε:

        $\varepsilon^k = \varepsilon^k {}^*10$; Go back to 2

    Else k = k + 1; $\varepsilon^k = \varepsilon^{k-1}/10$; Go back to 2

    End

End [20].

This approach improves the effect of numerical methods on the problem by adding a somewhat arbitrary regularization constant to help with the nonlinearity of the problem, but successfully so [13, 40]. We follow this procedure in our reconstruction algorithm, although alternatively we could have incorporated the manipulation of the scale factor and regularization constant in different preferential order. This convention was chosen over other possibilities since the linear least squares solution is exact and the scale factor is a sort of backup to ensure that a good search direction is not overlooked (i.e., possibly due to local inappropriateness of the linear approximation made by Gauss-Newton).

Dr. Arridge also uses regularization in his research, on both the nonlinear problem *and* on each iteration of the linearized version. He uses Marquardt regularization on his linearized problem, and a few other methods for regularizing the nonlinear cost function. A preliminary method regularizes by limiting the number of iteration steps; another is referred to as the 'truncated SVD,' and only includes the components of C_k which correspond to singular values above the signal to noise ratio. Since this truncation may neglect important information, a more advanced method is employed which includes his choice of error norm (this is referred to as the χ^2 norm: the residual vector-transposed times the inverse of the covariance of the measured output potentials times the residual vector again).

To regularize he adds the norm of the solution vector times a regularization constant and an exponential weight called a 'profiling function' which penalizes an entry's distance from the center of the tissue medium. When this profiling function is equal to one, this term is referred to as the Tikhonov part of the regularization. Arridge uses another regularization constant which is multiplied by a penalty on the second derivative of the tissue parameters, to control the smoothness of the solution. This is referred to as Phillips-Twomey

76

regularization. Arridge finds the profiling function and Tikhonov regularization to exhibit the best image clarity [13, Section 6].

Our experimental simulations which relate to regularization expand on the sampling results from Chapter 4 and further use of regularization to observe the resulting improvement in the conditioning of $J_k^T J_k$. For current injections every one, two, and three nodes, the condition numbers of the regularized Jacobian matrices are all approximately equal to one, to two decimal places. Interestingly, they actually *decrease* slightly with fewer current injections. From one node to three nodes between each current injection, the condition numbers are 1.0057, 1.0036, and 1.0017. We think this small decrease may be due to the fact that the regularization constant stays the same for all three sampling rates, while the smallest singular value may not be shrinking as quickly as the largest one does from one node to three between each current injection.

We also measure the relationship between the matrices $J_k^T J_k$ due to different current injection intervals more extensively. We project the actual perturbation in conductance onto the column space of the right singular vector in the singular value decomposition of $J_k^T J_k$. If we define the right singular vector as w_k, then the projection is:

$$p_k = w_k^T * \delta G.$$

This projection places a metric on the distance between the actual solution and the solution space according to the matrix $J_k^T J_k$ [44]. By comparing the distance between this projection and the actual perturbation in conductance for the three possible sampling intervals, we can arrive at a relative measure of resolution, and can compare this resolution with the relative size of the condition numbers of C_k. Unfortunately, this number is the same for all the matrices $J_k^T J_k$, with or without regularization or a change in the number of injection current sites. This metric might be reexamined in future experiments.

5.4 The Generalized Inverse Problem: an Explicit Solution?

This section reconsiders the possibility of solving the nonlinear inverse problem directly. In particular, the prospect of creating a generalized partial inverse of **G** is addressed [14]. We know many of the resistor values which depend upon both scattering and absorption, but we also have some unknown conductances which depend on the absorption alone. If we keep the unknown, vertical resistors as variables, we can construct a generalized form for the inverse. We can then solve for the exact values of the vertical resistors by using equations which are assembled from experimental measurements due to all the possible combinations of injection and measurement sites [14]. The idea is to compute and use only a portion of the complete inverse because we are only really interested in its bottom left HxH block. Focusing on this smaller section narrows the scope of the problem, and eliminates a great deal of unnecessary calculation. When we substitute these vertical conductance variables and the actual values of the horizontal conductances into the explicit inverse, we are left with the same number of equations as unknowns. This leaves a much smaller problem to solve, except for the very first time that the conductance matrix is inverted, than that with which we began.

To compare with existing methods for solving the forward problem, we wrote a program which calculates the section of the explicit inverse in which we are interested, given *all* the horizontal and vertical conductances. When optimally coded, its number of computations is slightly less than that which MATLAB takes to solve the forward problem using Gaussian elimination. But less information is extracted in this explicit inverse formulation of the problem, since it only gives the output potentials; when instead using MATLAB to solve n equations in n unknowns, we would find all the potentials on the grid. We need them *all* in the form this study uses for the Jacobian.

This concept would be a useful approach to the problem if we were able to calculate, in variable form, the small section of the inverse in which we are

interested. But for the size of matrices we consider in this problem, that is unfeasible. It would involve the recursive computation of the inverses of many HxH matrices, and would become an extremely complicated expression. However, the benefit of using this formulation is that it directly addresses the nonlinearity of the problem in a single step, instead of searching for the solution over many iterations, where improperly settling on a local stationary point is a possibility.

5.5 Comparing the Performance of our Algorithm for the Inverse Problem with that of Dr. Arridge

An important measure of the success of the reconstruction algorithms which solve the inverse problem is the comparison offered by the more extensive research which has already been done in this area. We refer to the work of Dr. Simon Arridge of University College London, which is described in detail in Section 5.1.

Arridge places a large emphasis upon the choice of error norm. Whereas the cost function we minimize is the Euclidean norm of the error, Arridge prefers the χ^2-norm. In attempting to reconstruct data which he has generated using the Monte Carlo method, Arridge has a scattering coefficient of about 20 mm^{-1} and an absorption coefficient of .025 mm^{-1} for 'healthy' tissue. For perturbations, he increases the absorption coefficient to .25 mm^{-1}. In order to detect perturbations of less than 3mm in diameter within a 50 mm diameter circle which is discretized to 16x16, he must use 10^{10} or 10^{12} photons [13, Section 6]. This assumes perfect detection so adjustments should be made depending on the efficiency of the measurement apparatus. His measurement models are the log of integrated intensity and the average time of flight, and they require this same number of injected photons in the article we cite, but an exact size for the added absorbers is not given, which makes a performance comparison between our two studies difficult [13].

6. Conclusions and Future Explorations

Chapter 2 has demonstrated that the resistive grid model closely resembles measurements which were made experimentally. Although the experimental data are vague, the reproduction of the single dip in Figure 2.5, where there were double dips in the other three experiments, instills some confidence in the resistive grid model. This is especially so, considering that the double-dip simulations closely resemble the experimental data as well.

However, in some other simulations, approximations almost as good as those shown in Chapter 2 were produced using an absorption coefficient which was two orders of magnitude *larger* than the one used in those simulations. This suggests that a mapping of resistor values to optical parameters, which produces results similar to experimental percent changes in magnitude, may not provide the true correspondence we seek. Certainly, it is the product of the horizontal and vertical conductances which determines the space constant for the problem, so there may be an ambiguity in the scaling of these parameters [20, 48].

Some discrepancy in the performance of the circuit model may be attributed to the fact that, according to the diffusion approximation, the point source is supposed to be located at least one scattering length *within* the boundary. In our circuit model, the point source is right *along* the boundary, where it would be experimentally.

The improvement of the condition number with a decrease in the injection current-spacing, as discussed in Chapter 3, should also encourage optimism toward what future experiments might be able to resolve. It would be interesting to determine the asymptotic limit of this beneficial effect through further computer simulation.

It is difficult to directly compare our reconstruction experiments with those of Dr. Arridge. His biological anisotropy constant is much smaller, and it yields a scattering length which is of a different order of magnitude than is predicted by

the breast tissue data we have been using (Arridge's scattering length is the inverse of the transport cross section, which is $(\mu_s'+\mu_a)^{-1}$ mm = $(2+0.025)^{-1}$ mm, or about 0.5 mm [10]). Experiments conducted by Ertefai on breast tissue predict a scattering length of $(.2578)^{-1}$ mm, or about 4 mm [46]. This means that Arridge expects less attenuation from the tissue than is predicted for breast tissue in the source cited by Ertefai. The comparison is discussed further in the next section.

The 15-bit noise figure found in Chapter 5 is also encouraging. In fact, it may even be a pessimistic estimate since our reconstruction algorithm is not attempting to solve for the horizontal conductances, and therefore does not include the extra information which could be used by taking the Jacobian with respect to those conductances. This 15-bit measurement precision is possible in the A/D converter, as well as in the digital computation. However, this result relies on ideal collection of measurement data. It will probably require a slight improvement in the abilities of the reconstruction algorithm, possibly by enhancing the regularization technique, in order to compensate for unanticipated measurement noise and the use of a 16-bit A/D converter. This handicap should also be investigated quantitatively in order to have a full understanding of the problem's limitations.

Even when using the GMRES algorithm to solve the linear least squares problem, the reconstruction is slowed by the formation of the Jacobian. Performing the computational 'current injections' in parallel might speed up the process [48]. Even finite-difference formulations of the Jacobian require that many output measurements are made and are multiplied together, creating a bottleneck. But even for its difficulty in construction, the Jacobian matrix reveals a great deal of information about the problem, and is required of many iterative approaches. We think the choice of an iterative method is less relevant than a faster route to the Jacobian might be. The Gauss-Newton method seems to be adequately efficient and information-intensive for the reconstruction.

Without the computational means which enable the progression to finer discretizations, and eventually to three dimensions, it is difficult to envision that integrated intensity *alone* might reveal information on the required order of a few millimeters which is necessary to make the inexpensive, optical detector worthwhile. However, our success with reconstructing small perturbations with a realistically large amount of quantization noise suggests that it is computationally possible to reconstruct perturbations using actual experimental data: the model appears promising, but needs to be enlarged.

6.1 Further Explorations

Since Arridge's work is extensive, improvements on our research might consist of developing a better comparison between the two studies. It would be good to compare Arridge's minimum photon count result (at which he could successfully reconstruct added absorption) with our corresponding tolerable quantization noise result. The precise size of absorbers Arridge used should also be investigated so that a corresponding simulation can be conducted and compared with his result.

The issue of the absorption coefficient's altering the value of the horizontal resistors, as we describe in the derivation of the horizontal and vertical conductances, should be better understood and physically explained. Currently we rely on the mathematical correspondence between the finite difference formulation of the Laplacian and the node equations in defining the resistor values.

In further improvements, the Jacobian should be expanded to include the aforementioned change in horizontal resistor values. Further attempts may be made to speed up the formation of the Jacobian, especially if the Jacobian matrix is to be increased in size. The GMRES algorithm for solving linear systems might be used for this. In addition, the noise model should be improved

82

to correspond more closely to the noise we expect from the experimental apparatus.

The increased difficulty in reconstructing a vertical perturbation in conductance when only the vertical conductances are actually perturbed (as opposed to when both horizontal and vertical conductances are actually perturbed and only vertical conductances are reconstructed) should be investigated more thoroughly. If the Jacobian is expanded to include that of the potentials with respect to the change in horizontal conductances, it could be used to see that the same result (that of increased difficulty) still holds. The expanded Jacobian may help to show *why* it does or does not still hold.

When the reconstruction can be sped up, finer discretizations, deeper slabs of simulated tissue, and even three dimensions may be considered. It will be important to consider the tradeoff between the benefits of finer discretizations versus having too many unknowns in the problem.

Finally, the cylindrical tissue model, as proposed by Professor Horn, may allow for the investigation of a more appropriate geometry for breast cancer detection, and a full circle of injection and measurement sites would then be possible.

References

1. Muller, G. et al., *Medical Optical Tomography: Functional Imaging and Monitoring.* SPIE Optical Engineering Press, Bellingham, WA, 1993, p. 5.

2. Webster, J. G., ed., *Electrical Impedance Tomography.* Adam Hilger, New York, 1990.

3. Ishimaru, A., *Wave Propagation and Scattering in Random Media, Volume 1: Single Scattering and Transport Theory.* Academic Press, New York, 1978.

4. Case and Zweifel, *Linear Transport Theory.* Addison-Wesley Publishing Company, Reading, MA, 1967.

5. Bertsekas, D. P., *Nonlinear Programming.* Athena Scientific, Belmont, MA, 1995.

6. Kelley, C. T., *Iterative Methods for Linear and Nonlinear Equations.* Society for Industrial and Applied Mathematics, Philadelphia, 1995.

7. Park, J., Personal Communication.

8. Golub and Van Loan, *Matrix Computations, Second Edition.* The Johns Hopkins University Press, Baltimore, 1993.

9. Strang, G., *Introduction to Linear Algebra.* Wesley-Cambridge Press, Wellesley, 1993.

10. Arridge, S., "The Forward and Inverse Problems in Time Resolved Infra-Red Imaging," *Medical Optical Tomography: Functional Imaging and Monitoring.* SPIE Optical Engineering Press, Bellingham, WA, 1993, pp. 35-64.

11. Groenhuis, R., H. Ferwerda, and J. Bosch, "Scattering and absorption of turbid materials determined from reflection measurements. 1: Theory," *Applied Optics.* Volume 22, Number 16, August 1983.

12. Kaltenbach J P and Kaschke M 1993 Frequency- and time- domain modeling of light transport in random media *Medical Optical Tomography: Functional Imaging and Monitoring* ed G. Muller et al. (Bellingham, WA: SPIE) pp. 65-86.

13. Arridge, S. and Schweiger, M., "Inverse Methods for Optical Tomography," in *Proceedings of the 13th International Conference on Information Processing in Medical Imaging*, H. Barrett and A. Gmitro, eds. Springer-Verlag, West Germany, 1993, p. 259-277.

14. Horn, B.K.P., suggested this in a personal communication.

15. Haberman, R., *Elementary Applied Partial Differential Equations with Fourier Series and Boundary Value Problems.* Prentice Hall, Englewood Cliffs, NJ, 1983.

16. Barbour, R. et al., "A Perturbation Approach for Optical Diffusion Tomography Using Continuous-Wave and Time-Resolved Data", *Medical Optical Tomography: Functional Imaging and Monitoring.* SPIE Optical Engineering Press, Bellingham, WA, 1993, p.87-120.

17. Mead, C., *Analog VLSI and Neural Systems*, Appendix C, "Resistive Networks". Addison-Wesley Publishing Company, Reading, MA.

18. Lee, M., personal communication

19. Wyatt, J., "Lectures on Nonlinear Circuit Theory," MTL Publications, Massachusetts Institute of Technology, 1992.

20. Wyatt, J., personal communication.

21. Graber, Chang, Aronson, and Barbour, "A Perturbation Model for Imaging in Dense Scattering Media: Derivation and Evaluation of Imaging Operators," *Medical Optical Tomography: Functional Imaging and Monitoring."* SPIE Optical Engineering Press, Bellingham, WA, 1993,p. 121-143.

22. Wyatt, J., "Little-Known Properties of Resistive Grids that are Useful in Analog Vision Chip Designs," *Vision Chips: Implementing Vision Algorithms with Analog VLSI Circuits*, C. Koch and H. Li, eds. IEEE Computer Society Press, Los Alamitos, CA, 1995.

23. Edelman, Alan., personal communication.

24. Arridge, S. et al., "Aspects of Clinical Infra-red Absorption Imaging," from *The Formation, Handling, and Evaluation of Medical Images*, Pokropek and

Viergever, eds. NATO ASI Series F, pp. 407-418, Springer-Verlag, Heidelberg, 1992.

25. Arridge, S., "Iterative Reconstruction of Near Infra-Red Absorption Images," SPIE Vol. 1767, *Inverse Problems in Scattering and Imaging*, 1992, pp. 372-383.

26. Arridge, S., "A Finite Element Approach for Modeling Photon Transport in Tissue," *Medical Physics*, Vol. 20, No. 2, Pt. 1, Mar/Apr 1993, pp. 299-309.

27. Koch, C. and H. Li, eds., *Vision Chips: Implementing Vision Algorithms with Analog VLSI Circuits.* IEEE Computer Society Press, Los Alamitos, CA, 1995.

28. White, Jacob, personal communication.

29. Strang, G., *Introduction to Applied Mathematics.* Wellesley-Cambridge Press, Wellesley, MA, 1986.

30. Arridge, S., "Photon-measurement density functions. Part 1: Analytical forms," *Applied Optics*, Vol. 34, No. 31, 1 November 1995.

31. Arridge, S. and M. Schweiger, "Photon-measurement density functions. Part 2: Finite-element-method calculations," *Applied Optics* Vol. 34, No. 34, 1 December 1995, pp. 8026-8037.

32. Arridge, S., M. Cope, and D. Delpy, "The theoretical basis for the determination of optical pathlengths in tissue: temporal and frequency analysis," *Physics in Medicine and Biology*, 1992, Vol. 37, No. 7, pp. 1531-1560.

33. Beuthan, J. et al., "Infrared diaphanoscopy (IRD) and infrared fluoroscopic imaging (IRF) in biological tissue," SPIE vol. 1888, pp. 517-528.

34. Hiraoka, M. et al., "A Monte Carlo investigation of optical pathlength in inhomogeneous tissue and its application to near-infrared spectroscopy," *Physics in Medicine and Biology* Vol. 38, 1993, pp. 1859-1876.

35. Sodini, C., personal communication.

36. Horn, R. and C. Johnson, *Topics in Matrix Analysis.* Cambridge University Press, New York, 1994, p. 113.

37. Arridge, S.R., M. Hiraoka, and M. Schweiger, "Statistical Basis for the Determination of Optical Pathlength in Tissue, *Physics in Medicine and Biology*. Volume 40, pp. 1539-1558, 1995.

38. Shewchuk, J.R., *An Introduction to the Conjugate Gradient Method Without the Agonizing Pain, Edition 1.25*, August, 1994. School of Computer Science, Carnegie Mellon University.

39. Delpy, D.T., et al., "Estimation of Optical Pathlength through Tissue from Direct Time of Flight Measurement," *Physics in Medicine and Biology*. Volume 33, Number 22, p. 1433-1442, 1988.

40. Seber, G.A.F. and C.J. Wild, *Nonlinear Regression*. John Wiley & Sons, New York, 1989, Section 14.2.2.

41. Tausch, Johannes, personal communication.

42. Ertefai, S. and A.E. Profio, "Spectral Transmittance and Contrast in Breast Diaphanography, *Medical Physics*. Volume 12, Number 4, July/August, 1985, pp. 393-400.

43. Moes, C.J.M. et al., "Measurements and Calculations of the Energy Fluence Rate in a Scattering and Absorbing Phantom at 633 nm," *Applied Optics*. Volume 28, Number 12, 15 June 1989, pp. 2292-2296.

44. Defrise, M., "Regularization Techniques in Medical Imaging," *Medical Images: Formation, Handling, and Evaluation*, A.E. Todd-Pokropek and M.A. Viergever, eds. NATO ASI Series F, Springer-Verlag, Heidelberg, 1992, pp. 43-64.

45. Peters, V.G. et al., "Optical Properties of Normal and Diseased Human Breast Tissues in the Visible and Near Infrared," *Physics in Medicine and Biology*. Volume 35, Number 9, September, 1990, pp. 1317-1334.

46. Navarro, G.A. and A.E. Profio, "Contrast in Diaphanography of the Breast," *Medical Physics*, Volume 15, Number 2, Mar/Apr, 1988, pp. 181-187.

47. Stoer, J. and R. Bulirsch, *Introduction to Numerical Analysis*. Springer-Verlag, New York, 1980, Section 8.2.

48. McQuirk, I., personal communication.

49. Oppenheim, A. and R. Schafer, *Discrete-Time Signal Processing*. Prentice Hall, Englewood Cliffs, NJ, 1989, p. 122.

Appendix—MATLAB Code

```
% gen1.m
% Generates measured data for nominal experiment
% This version incorporates sparse matrix procedures
% 1 mm between each grid node
% This algorithm creates a specified conductance matrix which is dependent on
% the grid spacing, tank depth, scattering, and absorption.
% Output measurements are taken directly across from the input
% 1" tank

clear all;
format long e;

b=8;      % 8 bits quantization noise in the measurement

% Set the following parameters for each different experiment

d= 1;                          % Grid node spacing
x= 120/.3937007874;            % Length on the input and output sides: 3"
y= 10/.3937007874;             % Length from input to output:  1"
xx= round(x/d)+1;              % Length in # nodes
yy= round(y/d);                % ditto
sz= xx*yy;                     % Size of conductance matrix

% Absorption coefficients:

a1= .002;                      % Nominal
a2= 1000;                      % Perturbed

% Transport cross section:

tr1= .39+a1;                   % The inverse of the effective space constant

% Horizontal conductance:

r1= 1/(tr1*d);                 % Conductance between neighboring nodes

% Vertical conductance:

g1= 3*a1*d;                    % Conductance from each node to ground
g2= 3*a2*d;                    % Perturbed conductance to ground

% First create the nominal conductance matrix:  see MATLAB sparse matrix info.

d1= zeros(1,sz)';              % d1= one band above the diagaonal
d1(2:sz)= -r1*ones(1,sz-1)';   % Conductance to neighbors 1 row above on grid
d_1= zeros(1,sz)';             % d_1= one band below the diagonal
d_1(1:sz-1)= -r1*ones(1,sz-1)'; % Conductance to neighbors 1 row below on grid
d0= zeros(1,sz)';              % Along the diagonal
d0(1:xx)= (3*r1)*ones(1,xx)';     % Input boundary has neighbors on three sides
d0(sz-xx+1:sz)= (3*r1)*ones(1,xx)'; % Interior has neighbors on four
d0(xx+1:sz-xx)= (4*r1)*ones(1,sz-2*xx)'; % Output boundary has neighbors on 3

% Create a boundary condition along the top and bottom of the grid:  there
% are only three neighbors there, too

for i= 1:yy
        d0((i-1)*xx+1)= d0((i-1)*xx+1)-r1; % Take one away from the top edge
        d0(i*xx)= d0(i*xx)-r1;             % and from the bottom edge
end

dxx= zeros(1,sz)';             % dxx= xx bands above the diagonal
dxx(xx+1:sz)= -r1*ones(1,sz-xx)'; % Cond. to neighbors 1 node to right on grid

d_xx= zeros(1,sz)';            % d_xx= xx bands below the diagonal
d_xx(1:sz-xx)= -r1*ones(1,sz-xx)'; % Cond. to neighbors 1 node to left on grid
```

```
for i= 1:yy-1
        d1(xx*i+1)= 0;              % Bottom edge does not connect to 1 row below
        d_1(xx*i)= 0;               % Top edge does not connect to 1 row above it
end

d0= d0+g1;                          % Add in conductance to ground at each node
B= [d_xx d_1 d0 d1 dxx];            % Create nonzero part of sparse matrix
clear d_xx d_1 d0 d1 dxx;           % Clear out unused variables
d= [-xx -1 0 1 xx]';                % Declare where these numbers go in the matrix
G= spdiags(B, d, sz, sz);           % Assemble sparse matrix based on those rules
clear B;                            % Now clear out B; don't need it anymore

% Conduct 'measurements' on this nominal conductance matrix

vm= [];                             % Initialize vector of measurements
for i= 1:xx                         % Prepare to inject at each input site
        inp= zeros(1,sz)';          % Create a zero vector for inp
        inp(i)= 1;                  % Make the site of injection equal to one
        v= G\inp;                   % MATLAB 'slash' for n equations in n unknowns
        vm= [vm' v(sz-xx+i)]';      % Add the ith output potential to the meas.
end
ns= vm./((sqrt(3))*2^(b+1));        % The actual noise stdev, according to # bits
vm= vm+ns.*randn(size(vm));         % Add it in, scaled by the nominal potential

save vm1 vm;                        % Store this vector in a .mat file
```

```
% This code produces the first experiment of the tank simulations
format long e;

b=8;                             % 8-bit quantization noise
ns= 1/((sqrt(3))*2^(b+1));       % The actual noise stdev, according to # bits


% Absorption coefficients:

a1= .002;                        % Nominal
a2= 1000;                        % Perturbed


% Transport cross section:

tr1= .39+a1;                     % The inverse of the effective space constant
tr2= .39+a2;


% Set the following parameters for each different experiment
d= 1;
x= 120/.3937007874;              % Length on the input and output sides (mm)
y= 10/.3937007874;               % Length from input to output
xx= round(x/d)+1;                % Number of nodes on input side
yy= round(y/d);                  % Number of nodes from input to output
sz= xx*yy;                       % Height/Width of the conductance matrix

absloc= [12*xx+142 12*xx+143 12*xx+163 12*xx+164 11*xx+142 11*xx+143 ...
11*xx+163 11*xx+164];                       % Absorber locations (node numbers)

% Horizontal conductance:

r1= 1/(tr1*d);
r2= 1/(tr2*d);

% Vertical conductance:

g1= 3*a1*d;
g2= 3*a2*d;


% First create the nominal conductance matrix:  uses MATLAB's sparse matrix

d1= zeros(1,sz)';                % d1= one band above the diagaonal
d1(2:sz)= -r1*ones(1,sz-1)';     % Conductance to neighbors 1 row above on grid
d_1= zeros(1,sz)';               % d_1= one band below the diagonal
d_1(1:sz-1)= -r1*ones(1,sz-1)';  % Conductance to neighbors 1 row below on grid
d0= zeros(1,sz)';                % Along the diagonal
d0(1:xx)= (3*r1)*ones(1,xx)';    % Input boundary has neighbors on three sides
d0(sz-xx+1:sz)= (3*r1)*ones(1,xx)'; % Interior has neighbors on four
d0(xx+1:sz-xx)= (4*r1)*ones(1,sz-2*xx)'; % Output boundary has neighbors on 3


% Create a boundary condition along the top and bottom of the grid:  there
% are only three neighbors there

for i= 1:yy
        d0((i-1)*xx+1)= d0((i-1)*xx+1)-r1; % Take one away from the top edge
        d0(i*xx)= d0(i*xx)-r1;             % and from the bottom edge
end

dxx= zeros(1,sz)';               % dxx= xx bands above the diagonal
dxx(xx+1:sz)= -r1*ones(1,sz-xx)'; % Cond. to neighbors 1 node to right on grid

d_xx= zeros(1,sz)';              % d_xx= xx bands below the diagonal
d_xx(1:sz-xx)= -r1*ones(1,sz-xx)';% Cond. to neighbors 1 node to left on grid


for i= 1:yy-1
        d1(xx*i+1)= 0;           % Bottom edge does not connect to 1 row below
        d_1(xx*i)= 0;            % Top edge does not connect to 1 row above it
```

```
end

d0= d0+g1;                        % Add in conductance to ground
B= [d_xx d_1 d0 d1 dxx];          % Create nonzero part of sparse matrix
clear d_xx d_1 d0 d1 dxx;         % Clear out unused variables
d= [-xx -1 0 1 xx]';              % Declare where these numbers go in the matrix

% Now increase the absorption at the proper site(s)

B(absloc-xx,1)= B(absloc-xx,1) + r1 - r2;
B(absloc-1,2)= B(absloc-1,2) + r1 - r2;
B(absloc,3)= B(absloc,3) - g1 - 4*r1 + g2 + 4*r2;
B(absloc+1,4)= B(absloc+1,4) + r1 - r2;
B(absloc+xx,5)= B(absloc+xx,5) + r1 - r2;
G= spdiags(B, d, sz, sz);
clear B;

% Conduct measurements with added absorption

vn= [];
load vm1;                         % The nominal output potentials (see gen1.m)
for i= 1:xx                       % Source location
        inp= zeros(1,sz)';        % Initialize
        inp(i)= 1;                % 1 A at that location
        v= G\inp;                 % Solve sz equations in sz unknowns
        vn= [vn' v(sz-xx+i)+(ns*randn(1,1))*vm(i)]';
end      % Take output potential at node exactly opposite from source and add
min(100*(vn-vm)./vm);             % measurement noise depending on # bits
save f1 vn;                       % Store the result
figure(1);                        % Plot %change in magnitude against length (")
hold off;
stepsz= 12/(xx-1);
nchs= 0:xx-1;
nchs= nchs*stepsz;
subplot(311),plot(nchs,vm);
ylabel('(Volts)');
xlabel('(a) (Inches)');
subplot(312),plot(nchs,vn);
ylabel('(Volts)');
xlabel('(b) (Inches)');
subplot(313),plot(nchs,100*(vn-vm)./vm);
hold on;
xlabel('(c) (Inches)');
plot(nchs(142),-56,'+');          % Also plot experimental results
plot(nchs(143),-56,'+');
plot(nchs(163),-58,'+');
plot(nchs(164),-58,'+');
plot(nchs(153),-38,'+');
ylabel('(% change in magnitude)');
```

```
% Generates measured data for nominal experiment
% This version incorporates sparse matrix procedures
% 4 mm between each grid node
% This algorithm creates a specified conductance matrix which is dependent on
% the grid spacing, tank depth, scattering, and absorption.
% Output measurements are taken directly across from the input

clear all;
format long e;

% Set the following parameters for each different experiment

d= 4;
x= 30/.3937007874;                  % Length on the input and output sides: 3"
y= 10/.3937007874;                  % Length from input to output:  1"
xx= round(x/d)+1;
yy= round(y/d);
sz= xx*yy;            .

% Absorption coefficients:
a1= .0668;
a2= .1195;

% Transport cross section:

tr1= .2578;
tr2= .3039;

% Horizontal conductance:

r1= 1/(tr1*d);
r2= 1/(tr2*d);

% Vertical conductance:

g1= 3*a1*d;
g2= 3*a2*d;

% Vertical conductance:

g1= 3*a1*d;                         % Conductance from each node to ground
g2= 3*a2*d;                         % Perturbed conductance to ground

% First create the nominal conductance matrix:  see MATLAB sparse matrix info.

d1= zeros(1,sz)';                   % d1= one band above the diagaonal
d1(2:sz)= -r1*ones(1,sz-1)';        % Conductance to neighbors 1 row above on grid
d_1= zeros(1,sz)';                  % d_1= one band below the diagonal
d_1(1:sz-1)= -r1*ones(1,sz-1)';     % Conductance to neighbors 1 row below on grid
d0= zeros(1,sz)';                   % Along the diagonal
d0(1:xx)= (3*r1)*ones(1,xx)';       % Input boundary has neighbors on three sides
d0(sz-xx+1:sz)= (3*r1)*ones(1,xx)'; % Interior has neighbors on four
d0(xx+1:sz-xx)= (4*r1)*ones(1,sz-2*xx)'; % Output boundary has neighbors on 3

% Create a boundary condition along the top and bottom of the grid:  there
% are only three neighbors there, too

for i= 1:yy
        d0((i-1)*xx+1)= d0((i-1)*xx+1)-r1; % Take one away from the top edge
        d0(i*xx)= d0(i*xx)-r1;             % and from the bottom edge
end

dxx= zeros(1,sz)';                  % dxx= xx bands above the diagonal
dxx(xx+1:sz)= -r1*ones(1,sz-xx)';   % Cond. to neighbors 1 col. to right on grid

d_xx= zeros(1,sz)';                 % d_xx= xx bands below the diagonal
```

94

```
d_xx(1:sz-xx)= -r1*ones(1,sz-xx)'; % Cond. to neighbors 1 col. to left on grid

for i= 1:yy-1
        d1(xx*i+1)= 0;              % Bottom edge does not connect to 1 row below
        d_1(xx*i)= 0;              % Top edge does not connect to 1 row above it
end

d0= d0+g1;                          % Add in conductance to ground
B= [d_xx d_1 d0 d1 dxx];            % Create nonzero part of sparse matrix
clear d_xx d_1 d0 d1 dxx;           % Clear out unused variables
d= [-xx -1 0 1 xx]';                % Declare where these numbers go in the matrix
G= spdiags(B, d, sz, sz);           % Assemble sparse matrix based on those rules
clear B;                            % Now clear out B; don't need it anymore

% Conduct 'measurements'

vm= [];                             % Initialize vector of measurements
vnom= [];
for i= 1:xx                         % Prepare to inject at each input site
        inp= zeros(1,sz)';          % Create a zero vector for inp
        inp(i)= 1;                  % Make the site of injection equal to one
        v= G\inp;                   % MATLAB 'slash' for n equations in n unknowns
        vm= [vm v(sz-xx+i)];        % Add the ith output potential to the meas.
        vnom= [vnom' v(sz-xx+1:sz)]';
end

save vm4 vm vnom;                   % Store this vector in a .mat file
```

```
% gn4dynamic.m
% This algorithm performs gauss-newton reconstruction with d= 4mm spacing,
% and a noise figure based on a nominal potential which sets the dynamic gain
% on an A/D converter with b bits.
% There is also a Marquardt method for finding the best regularization
% constant, starting with 0.01 and moving
% it up and down as it improves the size of the residual.


%b= 7;                      % # of bits, which determines the measurement noise


epsilon= 0.01;           % Regularization constant
absloc= [2*xx+7 2*xx+12];
                           % Location of perturbations in absorption


% Stage 1:  Begin w/ Nominal Absorption
% This is the first estimate of the linearly incremented conductance, so pot.
% is vguess, the potential with the perturbation we have so far.
% Conduct several current injections:

[v_all, e_all, vguess]= inject(1,xx,yy,sz,G); % inject.m is another function
vnom= vguess;            % Exact nominal potential
ns= vnom./((sqrt(3))*2^(b+1)); % The actual noise stdev, according to # bits
vnom= vnom+ns.*randn(size(vnom)); % Noisy measurement of nominal potential
                           % This is the 'dynamic gain' part.  It
                           % optimizes the performance of A/D converter


ddg= [];                 % Initialize vector of updates to conductance G
error= [];               % Initialize error vector to accumulate at each iter.
Guni= G;                 % Store the uniform conductance matrix


% Now perturb the conductance matrix, according to new optical parameters

[B,d]= spdiags(G);       % Take apart the sparse matrix
B(absloc,3)= B(absloc,3) - g1 + g2; % This line is for only perturbing the
                           % vertical conductance
G= spdiags(B, d, sz, sz);         % Put sparse matrix back together
fG= full(G);                      % Loses sparseness here for plotting;
dg= diag(fG);                     % could improve by re-sparsifying after
dmat= [];                         % plot.
for i= 1:yy
        dmat= [dmat dg((i-1)*xx+1:i*xx)];
end
figure(1);
mesh(dmat);
clear B;                 % Done with this; clear it out to save space
clear fG;
vmeas= [];               % Initialize measurement vector
for num= 1:xx            % Have to inject at every input node and record output
        input= [zeros(1,sz)]';   % Initialize current vector
        input(num)= 1;   % vmeas is a vector of length xx*xx; same throughout
        v=G\input;       % Measurement; note noise added two lines down
        % For each injection k, there are xx observations j
        vmeas= [vmeas' v(sz-xx+1:sz)'+ns((num-1)*xx+1:num*xx)'.*randn(1,xx)]';
end                      % append xx observed output nodes for each injection

vmeasavg= (sum(abs(vmeas)))/(xx*xx);    % Take an average of measured value
dv2jk= vmeas-vguess;     % The experimental potential minus that with uni. abs.
error= (sum(abs(dv2jk)))/(xx*xx);


% Now back to nominal G:

G= Guni;


% This section takes the v calculated from the nominal G and forms the
% products ejvkT which will be used to make the first guess at dG.
```

```
ejvkT= [];                      % Initialize estimated Jacobian
for k= 1:xx
        vk= [];                 % Reinitialize new vk for this set of ej's
        vk= v_all(:,k);         % Take the potentials due to input injections
        for j= 1:xx             % 30 observations for each injection
                ej= [];  % Reinitialize this ej
                ej= e_all(:,j);
                tmpv= ej.*vk;                   % Add this row to the estimated Jac.
                ejvkT= [ejvkT' tmpv]';  % Assemble xx*xx rows of eqns
        end
end
ejvkT1= ejvkT;                  % In some cases, we would like to know what the
                                % first Jacobian was, and not what it was at the end
                                % after many iterations.


% Now, the first dG, the dG which is linearized from uniform absorption:

prodJ= ejvkT'*ejvkT;    % Form the inner product of Jacobian...
dG= -diag((prodJ+epsilon*eye(min(size(ejvkT)))))\(ejvkT'*dv2jk)); %Least squares
oldG= G;                        % Save the old G in case this dG is too big and has to
                                % be scaled down
G= dG+G;                        % Create the first update to G
ddg= [ddg sqrt(sum((diag(dG)).^2))];    % Store the magnitude of update


% Stage 2:  Successive iterations of the linearization
% Let's try the dG we just got, and subsequent ones, and add them in if
% small enough to decrase the residual; otherwise we scale epsilon down by a
% factor of 1/10 until they are small enough to improve the error


iter= 0;                        % Counts number of iterations of the second stage
lvec= [1];                      % Initialize the vector of lambdas which scale dG
lambda= 1;
while iter < 470                % Stop after a certain number of iterations
        improving= 0;   % Set this constant to 0 until error improves, then 1
        try= 1;         % Scaling trial # is also reset
        lambda= lvec(length(lvec));     % The last lambda; scales epsilon
        while improving == 0
            [v_all, e_all, vguess]= inject(1,xx,yy,sz,G);
            dv2jk= vmeas-vguess;  % Calculate new difference between meas&guess
            error= [error (sum(abs(dv2jk)))/(xx*xx)]; % Also accumulate errors
            if (error(length(error)) < error((length(error))-1)) | ...
                (error(length(error)) == error((length(error))-1))
                    improving= 1;               % If the error is lower or same, done
                    figure(2);                  % Plot this G since it's a good one
                    dg= diag(G);
                    dmat= [];
                    for i= 1:yy
                            dmat= [dmat dg((i-1)*xx+1:i*xx)];
                    end
                    mesh(dmat);
                    lvec= [lvec lambda/10];% Keep track of lambda
            else                                % Otherwise scale down the guess; try
                if try<10                       % this ten times before new reg. const.
                    G= oldG+(.5^try)*dG;
                    try= try+1;
                    error= error(1:((length(error))-1));
                else
                    lambda= lambda*10;
                    % If it didn't go down, increase lambda
                    lvec(length(lvec))= lambda;
                    error= error(1:((length(error))-1));
                    % Take away old error term
                    dG= -diag((prodJ+lambda*epsilon*...
                    eye(min(size(ejvkT)))))\(ejvkT'*dv2jk));
                    G= oldG + dG;       % Go back to nominal G and halve the dG
                    try= 1;
```

```
                          end
                    end
           end        % Coming out of that last loop means now have a good, new G
           ejvkT= [];               % We have all injection sites from last part,so
           for k= 1:xx              % Make a new guess from that nominal
                   vk= [];          % Reinitialize new vk for this set of ej's
                   vk= v_all(:,k);  % Take the first set of potentials
                   for j= 1:xx      % 30 observations for each injection
                           ej= []; % Reinitialize new ej
                           ej= e_all(:,j);
                           tmpv= ej.*vk;
                           ejvkT= [ejvkT' tmpv]'; % Assemble xx*xx rows of eqns
                   end
           end
           prodJ= ejvkT'*ejvkT;
           dG= -diag((prodJ+lambda*epsilon*eye(min(size(ejvkT))))\(ejvkT'*dv2jk));
           ddg= [ddg sqrt(sum((diag(dG)).^2))];
           oldG= G;                 % Save nominal G
           G= G+dG;                 % Update G with new dG (for trial)
           iter= iter+1;            % Update number of improvements
           figure(3);
           subplot(311),plot(log10(ddg));
           ylabel('log10||dG||');
           subplot(312),plot(log10(error));
           ylabel('log10(error)');
           subplot(313),plot(log10(lvec));
           ylabel('log10(lambda)');
end

stepsz= 3/(xx-1);
nchs= 0:xx-1;
nchsy= nchs*stepsz;
stepsz= 1/(yy-1);
nchs= 0:yy-1;
nchsx= nchs*stepsz;
dg= diag(G);
                   dmat= [];
                   for i= 1:yy
                           dmat= [dmat dg((i-1)*xx+1:i*xx)];
                   end
                   mesh(nchsx, nchsy, dmat);
ylabel('Input Edge (Inches)');
xlabel('Depth (Inches)');
zlabel('Reconstructed Diagonal of the Conductance Matrix (mho)');
%zlabel('Actual Diagonal of the Conductance Matrix (mho)');
```

```matlab
% inject.m
% This function finds the potentials everywhere along the grid for injections
% along the input side, and for injections along the output side .
% When assembled properly, these values compute the Jacobian matrix
% We also get vguess out of it, from which we can compute the change
% in output potential

function [v_all, e_all, vguess]= inject(numlayers,xx,yy,sz,G)
vguess= [];
v_all= [];
for layer= 1:numlayers
        for row= 1:xx              % Perform xx current injections to test dG
                vacc= [];
                input= zeros(1,numlayers*sz)';
                input((layer-1)*xx+row)= 1;
                % At each test, only the kth inputut current is 1
                v= G\input;
                % Where v is the new guess potential according to new G
                for layer= 1:numlayers
                        vguess= [vguess' v(layer*sz-xx+1:layer*sz)']';
                        vacc= [vacc' v((layer-1)*sz+1:layer*sz)']';
                end
                v_all= [v_all vacc]; % Use this later for the est. Jacobian
        end
end
e_all= [];
for layer= 1:numlayers
        for row= sz-xx+1:sz        % Perform xx current injections to test dG
                input= [zeros(1,numlayers*sz)]';
                input((layer-1)*xx+row)= 1;
                % At each test, only the kth inputut current is 1
                v= G\input;
                % Where v is the new guess potential according to new G
                vacc= [];
                for layer= 1:numlayers
                        vacc= [vacc' v((layer-1)*sz+1:layer*sz)']';
                end
                e_all= [e_all vacc];   % Use later for estimate of Jacobian
        end
end
```